JOURNAL OF GEOPHYSICAL RESEARCH, VOL. 105, NO. B5, PAGES 11,063–11,082, MAY 10, 2000

Role of temperature-dependent viscosity and surface plates in spherical shell models of mantle convection

Shijie Zhong and Maria T. Zuber

Department of Earth, Atmospheric and Planetary Sciences, Massachusetts Institute of Technology, Cambridge

Louis Moresi

Australian Geodynamics Cooperative Research Centre, CSIRO Exploration and Mining, Nedlands, Western Australia

Michael Gurnis

Seismological Laboratory, California Institute of Technology, Pasadena

Abstract. Layered viscosity, temperature-dependent viscosity, and surface plates have an important effect on the scale and morphology of structure in spherical models of mantle convection. We find that long-wavelength structures can be produced either by a layered viscosity with a weak upper mantle or temperature-dependent viscosity even in the absence of surface plates, corroborating earlier studies. However, combining the layered viscosity structure with a temperature-dependent viscosity results in structure with significantly shorter wavelengths. Our models show that the scale of convection is mainly controlled by the surface plates, supporting the previous two-dimensional studies. Our models with surface plates, layered and temperature-dependent viscosity, and internal heating explain mantle structures inferred from seismic tomography. The models show that hot upwellings initiate at the core-mantle boundary (CMB) with linear structures, and as they depart from CMB, the linear upwellings quickly change into quasi-cylindrical plumes that dynamically interact with the ambient mantle and surface plates while ascending through the mantle. A linear upwelling structure is generated again at shallow depths (<200 km) in the vicinity of diverging plate margins because of the surface plates. At shallow depths, cold downwelling sheets form at converging plate margins. The evolution of downwelling sheets depends on the mantle rheology. The temperature-dependent viscosity strengthens the downwelling sheets so that the sheet structure can be maintained throughout the mantle. The tendency for linear upwelling and downwelling structures to break into plume-like structures is stronger at higher Rayleigh numbers. Our models also show that downwellings to first-order control surface plate motions and the locations and horizontal motion of upwellings. Upwellings tend to form at stagnation points predicted solely from the buoyancy forces of downwellings. Temperature-dependent viscosity greatly enhances the ascending velocity of developed upwelling plumes, and this may reduce the influence of global mantle flow on the motion of plumes. Our results can explain the anticorrelation between hotspot distribution and fast seismic wave speed anomalies in the lower mantle and may also have significant implications to the observed stationarity of hotspots.

1. Introduction

Recent seismic tomography studies [*van der Hilst et al.*, 1997; *Grand et al.*, 1997; *Grand*, 1994; *Masters et al.*, 1996] have greatly improved our understanding of global mantle structure and dynamics. These studies show that down to a depth of 1800 km in the upper and middle mantle, structure can be characterized as linear slab-like features that are related to subduction [*Grand et al.*, 1997; *van der Hilst et al.*, 1997]. The bottom 1000 km of the mantle may display different morphology in which the linear features have disappeared [*van der Hilst and Karason*, 1999]. In the upper mantle, other features include fast wave speed anomalies down to a depth of 300 to 400 km beneath continental cratons and slow wave speed anomalies associated with spreading centers at relatively shallow depths [*Zhang and Tanimoto*, 1992; *Masters et al.*, 1996; *Grand et al.*, 1997]. In addition, these structures occur at wavelengths that are comparable with the scale of tectonic plates, consistent with early studies [*Su and Dziewonski*, 1992; *Fukao et al.*, 1992]. Regional tomography studies near Iceland and other hotspots have located plume structures extending to a depth of at least 400 km [*Wolfe et al.*, 1997; *Shen et al.*, 1998; *VanDecar et al.*, 1995]. Recent seismic studies with new techniques suggest that horizontal rolls may exist in the upper mantle below the Pacific Plate, aligned with the plate motion [*Katzman et al.*, 1998].

These studies provide a simple but important picture about the mantle: Plate motion controls mantle circulation, confirming the predictions from previous dynamic models

Paper number 2000JB900003.
0148-0227/00/2000JB900003$09.00

based on plate kinematics (referred to as kinematic models hereafter). It has been suggested that the motion of rigid tectonic plates has dominant effects on mantle flow owing to the coupling between plates and the mantle [*Hager and O'Connell*, 1979; *Davies*, 1988]. In particular, because creation and cooling of oceanic lithosphere associated with plate motion transport more than 80% of the heat out of the mantle, mantle flow and thermal structure must be dominated by plate-scale mode [*Davies and Richards*, 1992]. Recent numerical models in a spherical shell geometry with imposed plate motion produce cold downwellings which have some resemblances to the structure seen in seismic tomography [*Bunge et al.*, 1998].

Since surface plates are imposed in these kinematic models [e.g., *Bunge et al.*, 1998], substantial effort has been made to formulate self-consistent dynamic models of the mantle in order to interpret the large-scale seismic structure. Early spherical models at low Rayleigh numbers (Ra=10^4) with constant viscosity produced large-scale structure with linear downwelling sheets [*Bercovici et al.*, 1989]. At relatively high Ra (~10^6, still significantly smaller than the value appropriate for the Earth), including either an endothermic phase change at the 670 km [*Tackley et al.*, 1993] or a weak upper mantle [*Zhang and Yuen*, 1995; *Bunge et al.*, 1996], but still with no temperature-dependent rheology, produces long-wavelength structures. Neither isoviscous nor layered viscosity models produce surface plates. Temperature-dependent rheology with small activation energy can also produce long-wavelength structure, as shown in Cartesian models [*Tackley*, 1993, 1996]. However, as the activation energy increases (but still much smaller than a realistic value), stagnant lid convection develops and the structure wavelengths are dramatically reduced [*Ratcliff et al.*, 1997; *Christensen*, 1984; *Tackley*, 1993; *Moresi and Solomatov*, 1995; *Solomatov*, 1995]. Therefore, the mobility of tectonic plates suggests that a brittle rheology that facilitates plate motion by weakening plate margins may be important to the dynamics and structure of the mantle [*Gurnis*, 1989; *King and Hager*, 1990; *Bercovici*, 1993; *Puster et al.*, 1995; *Zhong and Gurnis*, 1994, 1996; *Gurnis et al.*, 2000]. The dynamics of plate margins and their relation to plate tectonics are an active research area [*Bercovici*, 1998; *Zhong et al.*, 1998; *Moresi and Solomatov*, 1998; *Tackley*, 1998].

The purpose of this paper is to study the influence of mantle rheology (layered viscosity, temperature-dependent viscosity, and surface plates) on the scales and morphology of mantle structure with spherical models of thermal convection. First, we will focus on the influences of layered viscosity structure coupled with a temperature-dependent viscosity and of surface plates with a weak zone formulation. Second, we will examine the morphology of downwellings and upwellings and their dependence on rheology and surface plates. Specifically, we will study the characteristic structures for upwellings and downwellings when they form and as they evolve during ascent or descent through the mantle under different conditions (i.e., Rayleigh number Ra, surface plates, and the rheology including constant, layered, and temperature-dependent viscosities). These questions are important for understanding the implications of structures revealed in seismic tomography [e.g., *van der Hilst and Karason*, 1999; *Van der Voo et al.*, 1999] to rheology and dynamics of the mantle. Using improved numerical and computational technology, our constant viscosity and temperature-dependent viscosity models will employ Ra higher than those by *Bercovici et al.* [1989], *Glatzmaier et al.* [1990], and *Ratcliff et al.* [1997]. Compared with previous kinematic models by *Bunge et al.* [1998] that only include a layered viscosity structure, our models include both temperature-dependent and layered viscosity structure and free slip boundary condition but with smaller Ra.

In the following sections we will first present the governing equations, a new finite element formulation used to solve the equations in a spherical geometry, and benchmarks with analytic solutions and other previously published numerical results. Second, we will present results from standard mantle convection models without surface plates. Third, flow and thermal structures for models with plates will be presented.

2. Model Formulation and Numerical Approach

2.1. Governing Equations

The mantle is treated as an incompressible viscous medium. Thermal convection in the mantle is governed by the conservation equations of mass, momentum, and energy.

$$u_{i,i} = 0, \tag{1}$$

$$-P_{,i} + (\eta u_{i,j} + \eta u_{j,i})_{,j} + \delta\rho g \delta_{ir} = 0, \tag{2}$$

$$T_{,t} + u_i T_{,i} = \kappa T_{,ii} + H, \tag{3}$$

where u_i is the velocity, P is the dynamic pressure, $\delta\rho$ is the density anomalies, g is the gravitational acceleration, η is the viscosity; T is the temperature, κ is the thermal diffusivity, H is the heat production rate, and $X_{,y}$ represents the derivative of X with respect to y, i and j are spatial indices, t is the time. The repeated indices represent summation. We ignore buoyancy forces associated with composition and phase changes. Therefore the density anomalies are

$$\delta\rho = -\alpha\rho_0 (T - T_0), \tag{4}$$

where α is the thermal expansivity, ρ_0 is a reference and T_0 is the surface temperature.

Substituting (4) into (2) and performing the following normalization:

$$x_i = R_o x_i', \quad u_i = \frac{\kappa}{R_o} u_i', \quad T = \Delta T T' + T_0,$$

$$t = \frac{R_o^2}{\kappa} t', \quad \gamma = \frac{H R_o^2}{\kappa \Delta T}, \quad \eta = \eta_0 \eta', \quad P = \frac{\eta_0 \kappa}{R_o^2} P', \tag{5}$$

where R_o is the Earth's radius, η_0 is a reference viscosity, ΔT is the superadiabatic temperature drop from the core-mantle boundary (CMB) to the surface. Dropping the primes, the equations become

$$u_{i,i} = 0, \tag{6}$$

$$-P_{,i} + (\eta u_{i,j} + \eta u_{j,i})_{,j} + \xi Ra T \delta_{ir} = 0, \tag{7}$$

$$T_{,t} + u_i T_{,i} = T_{,ii} + \gamma, \tag{8}$$

where Ra, a Rayleigh number, and ξ are defined as

$$Ra = \frac{\rho g \alpha \Delta T D^3}{\eta_o \kappa}, \quad \xi = \frac{R_o^3}{D^3}, \tag{9}$$

where D is the thickness of the mantle.

Equations (6)–(8) can be solved when the boundary and initial conditions are specified. The surface and CMB are subject to free slip and isothermal boundary conditions.

2.2. CitcomS: A Three-Dimensional Spherical Finite Element Code

For nonlinear and time-dependent thermal convection problems the governing equations can only be solved numerically. Because the finite element method (FEM) is extremely robust in treating complex material properties and geometry, we choose the FEM with a primitive variable (i.e., velocity and pressure) formulation [*Hughes*, 1987] to solve these equations in a three-dimensional (3-D) spherical shell geometry. The FEM has been widely used in studying mantle dynamics [*King et al.*, 1990; *Moresi and Gurnis*, 1996]. Both our numerical algorithms and the resulting FEM software, known as CitcomS, are extensions of a 3-D Cartesian FEM software Citcom [*Moresi and Gurnis*, 1996]. However, four additional developments have been made: spherical geometry, a new grid design, parallel computing, and a full multigrid algorithm. Because the new methodology is quite general and could be used in a variety of global geophysical studies, we present detailed analyses in a set of appendices with a briefed description given as follows.

Inherited from Citcom [*Moresi and Gurnis*, 1996], CitcomS employs a Uzawa algorithm to solve the momentum equation coupled with the incompressibility constraint (i.e., equation (6)) [*Ramage and Wathen*, 1994] and a streamline upwind Petrov-Galerkin method [*Brooks*, 1981] for solving the energy equation. Brick elements (i.e., eight velocity nodes with trilinear interpolation functions and one constant pressure node for each element) are used. The use of brick elements in 3-D (or rectangular elements in 2-D) is important for accurately determining the pressure (i.e., dynamic topography) in incompressible Stokes' flow [*Hughes*, 1987; *Bathe*, 1995].

The use of eight node brick elements means that the sphericity is only realized approximately for each individual element. However, as our benchmarks demonstrate, the resulting numerical error is insignificant even for a moderate resolution. Our numerical grid is designed to have relatively uniform resolution in both polar and equatorial regions, avoiding excessive resolution near the poles, a strategy that was demonstrated computationally efficient in the 3-D spherical convection code Terra [*Baumgardner*, 1985]. However, our gridding approach is different from that used in Terra because of the use of brick elements. We first divide a spherical surface into 12 cells of approximately equal size and then further divide each cell evenly into $N \times N$ elements (Figure 1). In the radial direction the grid spacing can be variable. Another advantage of such grids is that parallel computing is naturally embedded. On the basis of the highly efficient multigrid solver for the momentum equation in Citcom we further improve its efficiency by implementing a full multigrid algorithm [*Press* et al., 1992] with a consistent projection scheme in CitcomS.

2.3. Validation of CitcomS

We now prove the accuracy of the method by comparing results from CitcomS with analytic solutions and previously published numerical solutions for three different problems. The first problem is for Stokes' flow with layered viscosity

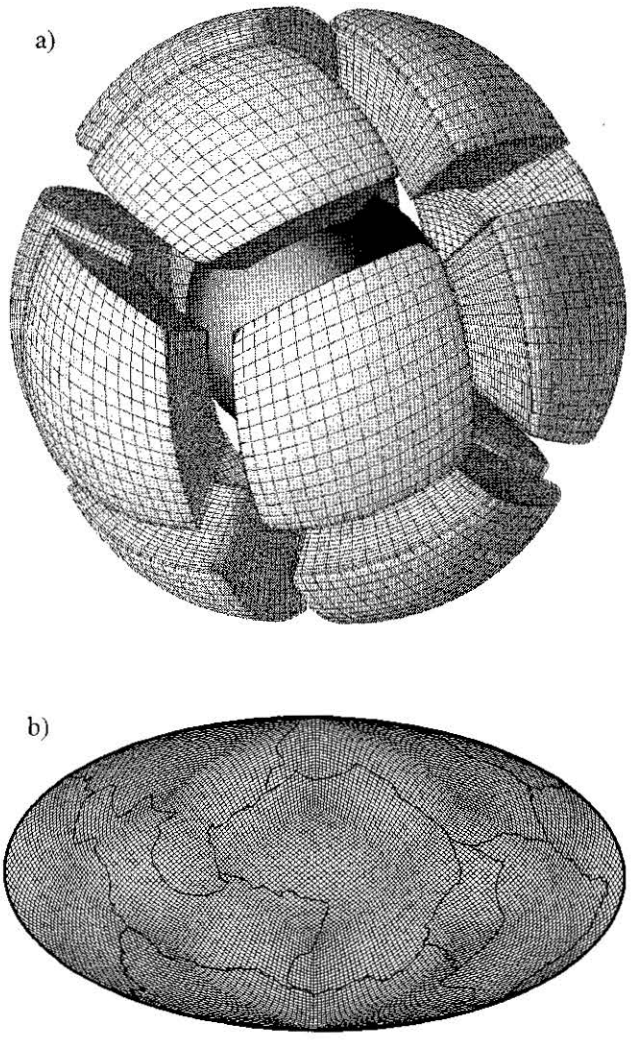

Figure 1. The three-dimensional grid used in CitcomS for decomposition in parallel computing (Figure 1a) and the finite element grid on a spherical surface and plate boundaries (Figure 1b).

structure for which analytic solutions can be obtained [e.g., *Hager and O'Connell*, 1981]. The second problem is for the dependence of critical Rayleigh number on spherical harmonic degree, which have been predicted from a linear stability analysis [*Chandrasekhar*, 1961]. The third problem is for finite amplitude thermal convection in isoviscous media, and for this problem, previously published results are available in the literature [*Bercovici et al.*, 1989; *Ratcliff et al.*, 1996]. While the first problem is used to verify our solver for the momentum and continuity equations, the second and third problems are for verifying our solvers for the three governing equations. The detailed definitions for these three problems are given in Appendix C.

For the first problem we use 32 elements in each dimension in each of 12 cells (the total number of elements is 12x32x32x32), and for the second problem, 24 elements in each dimension in each cell are used (Figure 1). Comparisons are given in Tables 1, 2, and 3. Table 1 shows that for Stokes' flow with both isoviscous and layered viscosity (10^4 viscosity contrast) structures both surface velocity and stress (i.e., dynamic topography) from CitcomS agree with analytic

Table 1. Benchmarks for the Stokes' Flow Problem

	η_1/η_2 *	(l, m)	V^s †	V^b	H^s_{rr}	H^b_{rr}
ANA †	1	(2, 0)	-1.0064×10^{-2}	1.1861×10^{-2}	-4.1919×10^{-1}	7.7058×10^{-1}
Error‡, %			0.44	0.30	0.32	0.38
ANA		(4, 0)	-5.2152×10^{-3}	5.7116×10^{-3}	-4.1462×10^{-1}	7.3709×10^{-1}
Error, %			0.28	0.10	0.53	0.84
ANA	10^4	(2, 0)	-6.1380×10^{-6}	4.0304×10^{-3}	-5.3411×10^{-1}	3.2094×10^{-1}
Error, %			--	0.40	0.55	0.32
ANA		(4, 0)	-1.4578×10^{-6}	2.7046×10^{-3}	-4.8059×10^{-1}	3.8212×10^{-1}
Error, %			--	0.31	1.0	0.57

* This is the viscosity contrast between the top and bottom layers. There are 32 elements uniformly distributed in the radial direction. The top layer spans five elements.

† Analytic solutions (ANA) are from propagator matrix techniques which can give coefficients of spherical harmonic function for boundary velocity (i.e., V^s, V^b) and normal stress (i.e., H^s_{rr}, H^b_{rr}) for surface and bottom boundaries.

‡ The error is relative difference between analytic and CitcomS solutions over the entire spherical surface on the top and bottom boundaries. The boundary velocity and normal stress from the propagator matrix method can be calculated with the coefficients V^s, V^b, H^s_{rr}, and H^b_{rr} (e.g., for the surface $V^s_\theta = V^s\,\partial Y_{lm}/\partial\theta$, $V^s_\varphi = V^s/\sin\theta\cdot\partial Y_{lm}/\partial\varphi$, and $\sigma^s_{rr} = H^s_{rr}Y_{lm}$ where Y_{lm} is the spherical harmonic function).

solutions to within 1%. This indicates that CitcomS can be used in studying the geoid problem [*Zhong and Davies*, 1999]. In fact, we have reproduced the geoid obtained from analytic models by *Ricard et al.* [1993] with the same viscosity and density structure [*Zhong and Davies*, 1999]. Table 2 shows a similar accuracy of CitcomS in predicting critical Rayleigh numbers for spherical harmonic degrees from 2 to 9 (note the consistently small errors, all < 1%, for all the degrees). For finite amplitude thermal convection problems the Nussult numbers from CitcomS agree well with those previously published results (Table 3). These are the Nussult numbers in the steady state and are determined by solving the time-dependent energy equation until the relative variation in the Nussult number between two consecutive time steps is smaller than 10^{-5}.

2.4. Description of Models

We will present models with different viscosity structure: constant viscosity, temperature-dependent viscosity, layered viscosity, and a plate rheology. A nondimensional temperature-dependent viscosity is given as [e.g., *Ratcliff et al.*, 1996]

$$\eta = A\exp[E(0.5-T)], \tag{10}$$

where A can be a function of radius for simulating a layered viscosity and E is the parameter controlling the magnitude of viscosity variations due to temperature variations and is equivalent to the activation energy. A viscosity at T=0.5 with preexponential constant A in the lower mantle is used to define a Rayleigh number in (9).

For diffusion creep in olivine as determined from laboratory studies [e.g., *Karato and Wu*, 1993], the activation energy is ~ 300 KJ/mol. Studies of surface deflection of oceanic lithosphere near seamounts suggest smaller activation energies [*Courtney and Beamount*, 1983] particularly with newly compiled data [*Watts and Zhong*, submitted, 1999]. The activation energy implies a rapid increase in viscosity by several tens of orders of magnitude from mantle to surface temperatures. However, the high-viscosity regions are concentrated near the surface where deformation is controlled by brittle rather than viscous deformation. Therefore we will use relatively smaller activation energies to achieve moderate viscosity variations (< 10^5), which are also numerically tractable. Since brittle deformation is only important at plate margins, we represent plate margins with weak zones while the rest of media is represented with layered and temperature-dependent viscosity (Figure 1). The combination of weak zones and temperature-dependent viscosity represents a

Table 2. Benchmarks for the Critical Rayleigh Number Ra_{cr}

	Spherical Harmonic Degree							
	2	3	4	5	6	7	8	9
Ra_{cr} (CitcomS)	8875.0	7850.0	8875.0	11245	15050	20500	28000	37950
Ra_{cr} (L.S.A.)*	8820.0	7880.0	8940.0	11350	15180	20630	28060	37820
Error, %	0.62	0.38	0.73	0.93	0.86	0.63	0.21	0.34

* Ra_{cr} for the linear stability analysis (L.S.A.) are from *Chandrasekhar* [1961]. *Ra* here are defined with the outer radius of a spherical shell.

Table 3. Comparison of Nussult Numbers *Nu*

	CitcomS		*Bercovici et al.* [1989]		*Ratcliff et al.* [1996]
Ra	Nu_{top}	Nu_{bot}	Nu_{top}	Nu_{bot}	Nu_{top}
2000	2.218	2.201	2.2507	2.2532	2.1740
7000	3.519	3.472	3.4657	3.5293	3.4423

For each case, Nussult numbers for both surface and bottom boundaries are listed. Ideally, they should be the identical. The results for *Bercovici et al.* [1989] are from their AS code. *Ratcliff et al.*, [1996] did not give Nussult numbers for bottom boundary.

reasonable approximation to plate rheology [e.g., *Davies*, 1989; *Gurnis*, 1989]. In our models with plates the weak zones are assumed to be 500 km wide and have a viscosity that is the same as the average viscosity within the upper mantle (from 100 to 400 km in depth). The width of weak zones is ~ 2 times the thickness of thermal boundary layer in our models, and this is chosen so that weak zones can effectively decouple surface plates [*King and Hager*, 1990]. We also assume that weak zones do not evolve with time.

The thickness of the mantle is assumed to be 2867 km (the nondimensional thickness is 0.45). This leads to $\xi = 10.974$ in (9). Thermal expansivity, diffisivity, and heat production rate are assumed to be constant. In models with internal heating, the nondimensional heat production rate γ is 60, and this is equivalent to about half of heat production rate for the Earth's bulk mantle [*Turcotte and Schubert*, 1982]. We integrate the models for at least four transit times to obtain statistically stable solutions of flow and thermal structures.

To quantify our model results, we define divergence and radial vorticity for surface velocity as [*Forte and Peltier*, 1987]

$$S(\theta,\phi) = \frac{1}{r\sin\theta}\left[\frac{\partial(\sin\theta V_\theta)}{\partial\theta} + \frac{\partial V_\phi}{\partial\phi}\right], \quad (11)$$

$$\omega(\theta,\phi) = \frac{1}{r\sin\theta}\left[\frac{\partial(\sin\theta V_\phi)}{\partial\theta} - \frac{\partial V_\theta}{\partial\phi}\right], \quad (12)$$

where r, θ, and ϕ are the radial, latitudinal and longitudinal coordinates, respectively, and V_θ and V_ϕ are the latitudinal and longitudinal components of surface velocity. We define residual temperature field as

$$\delta T(r,\theta,\phi) = T(r,\theta,\phi) - \frac{1}{4\pi}\oint_{\theta,\phi} T(r,\theta,\phi)\sin\theta d\theta d\phi, \quad (13)$$

where the second term of the right-hand side is the average temperature at radius r. This residual temperature is often used to characterize 3-D thermal structure [e.g., *Tackley*, 1996]. To better quantify the radial dependence of structure, we use the temperature to define an average aspect ratio A_r and length L for downwelling and upwelling structures at each depth. In defining A_r we first identify individual upwelling and downwelling structures at each depth. A downwelling (upwelling) structure is the region in which the temperature is one third below (above) the average temperature at that depth (the particular choice of one third for the threshold does not influence the results significantly). Each downwelling (upwelling) structure has a minimal separation of 5° between themselves. Once a structure is determined, we can determine its width and length (e.g., the maximum distance between any two points within the structure) from which aspect ratio for this structure can be computed. L and A_r for downwellings (upwellings) at this depth are the weighed average length and aspect ratio for all the downwelling (upwelling) structures. A_r is unity if all the structures are cylindrical plumes.

3. Results

3.1. Models With Constant Viscosity

We first present two cases with constant viscosity and internal heating at different Rayleigh numbers (Table 4). For case 1 with Ra=2.43x10^5, the internal heating rate determined a posteriori from the average surface and bottom heat fluxes is ~ 60% (Table 4). The thermal structure for both downwellings and upwellings varies with depth (Plate 1a). Near the surface, the downwellings form long linear sheets that surround upwelling plumes. However, the linear sheets break into plume-like structure at relatively shallow depths. Near the bottom of the mantle, the downwellings remain plume-like and are surrounded by long linear upwellings (Plate 1a). Like downwellings, the linear upwellings break into cylindrical structures as they ascend from the CMB (Plate 1a). The structural aspect ratio A_r for downwellings is > 20 near the surface but it decreases rapidly with depth to ~ 2. A_r for upwellings is symmetric with that for the downwellings (Figures 2a and 2b).

The thermal structure is also dependent on Ra or the vigor of convection [e.g., *Tackley*, 1996]. Case 2 differs from case 1 in having a Ra that is 3 times higher. The higher Ra leads to thermal structures with reduced wavelengths or spacings between upwellings and downwellings (Plate 1b). Spectra of

Table 4. Model Parameters

Case	Plates	E	η_{lm}/η_{um}	γ	Ra	ζ, %	H_s
1	N	0	1	60	2.43E5	60	22.36
2	N	0	1	60	7.29E5	51	27.74
3	N	0	30	60	2.43E4	74	20.65
4	N	0	30	60	2.43E5	70	35.84
5	N	6.9078	1	60	7.29E5	31	19.15
6	N	6.9078	30	60	2.43E5	67	32.69
7	Y	9.2025	60	60	2.43E5	61	27.29
8	Y	0	60	60	4.0E5	61	22.22

E is the nondimensional activation energy; η_{lm}/η_{um} is the ratio of the lower mantle to upper mantle viscosities; γ is heat production rate; Ra is a Rayliegh number; ζ and H_s are internal heating rate and surface Nusselt number. Ra is defined by the lower mantle viscosity for layered viscosity models (cases 3, 4 and 8). Ra for temperature-dependent viscosity models (cases 5, 6 and 7) is defined by viscosity at T=0.5 in the lower mantle. Read 2.43E5 as 2.43x10^5.

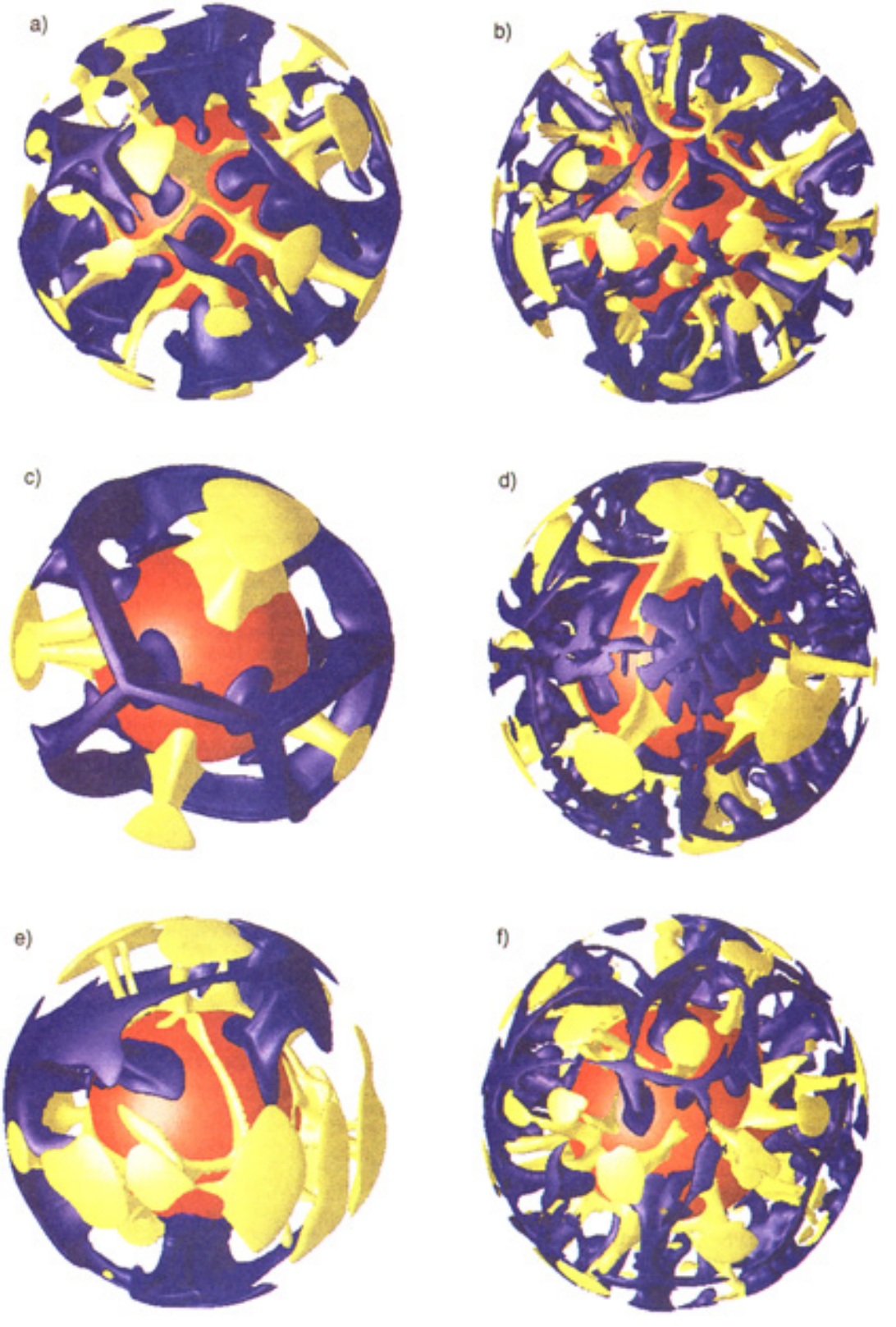

Plate 1. Isosurfaces for residual temperature for isoviscous (Plates 1a and 1b for cases 1 and 2, respectively), layered viscosity (Plates 1c and 1d for cases 3 and 4, respectively), temperature-dependent viscosity (Plate 1e for case 5), and layered viscosity coupled with temperature-dependent viscosity (Plate 1f for case 6). Yellow isosurfaces represent δT=0.12 (i.e., above the average temperature), and blue isosurfaces represent δT=-0.12, except for Plate 1d in which the blue isosurfaces are for δT=-0.08.

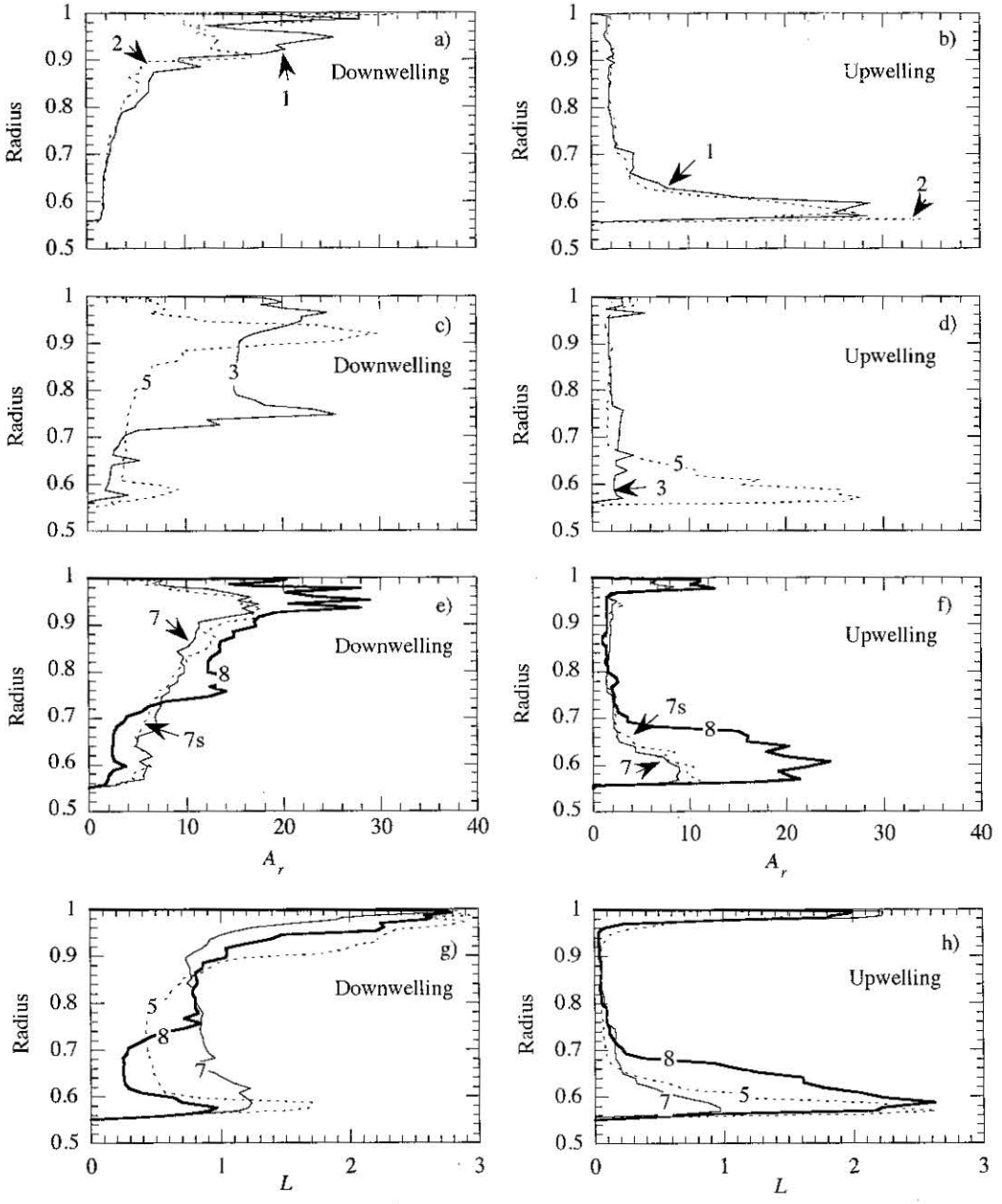

Figure 2. Radial dependence of average structural aspect ratio A_r for downwellings (Figures 2a, 2c, and 2e) and upwellings (Figures 2b, 2d, and 2f) for cases 1-3, 5, 7, and 8. In Figures 2e and 2f, the dashed lines labelled with 7s are for case 7 with 1/4 as the threshold in defining the structures. Figures 2g and 2h are the radial dependence of average structural length L for downwellings and upwellings, respectively.

the temperature field show that power peaks at l=10 and 12 near the surface and the bottom of the mantle, respectively (Figures 3a and 3b for cases 1 and 2, respectively). Downwellings (upwellings) within the mantle in case 2 break into plume-like structure quicker as they leave the thermal boundary layers (TBL), as indicated by A_r (Figures 2a and 2b). With smaller *Ra*, *Glatzmaier et al.* [1990] and *Ratcliff et al.* [1997] have found similar downwelling structure that extends to a greater depth. Our results show that the depth to which linear downwellings extend reduces with increasing *Ra*. The variations of thermal structure with depth from our models are also consistent with that found in 3D Cartesian models with entirely internal heating at high *Ra* (~ 10^7) [*Parmentier et al.*, 1994].

In both cases 1 and 2 the average horizontal velocity V_h is similar in magnitude in the top and bottom TBL, implying similar thickness for these two TBL (Figures 4a and 4b). Case 1 with smaller *Ra* has a smaller V_h but higher mantle temperature, compared with case 2 (Figure 4a).

3.2. Models With Layered Viscosity

Much attention has been given to the influence of a layered viscosity structure on thermal structure [*Zhang and Yuen*, 1995; *Bunge et al.*, 1996, 1997], because a weak upper mantle explains the geoid anomalies and post-glacial rebounding data [*Hager and Richards*, 1989; *Mitrovica and Forte*, 1997]. Cases 3 and 4 employ a layered viscosity structure in which the lower

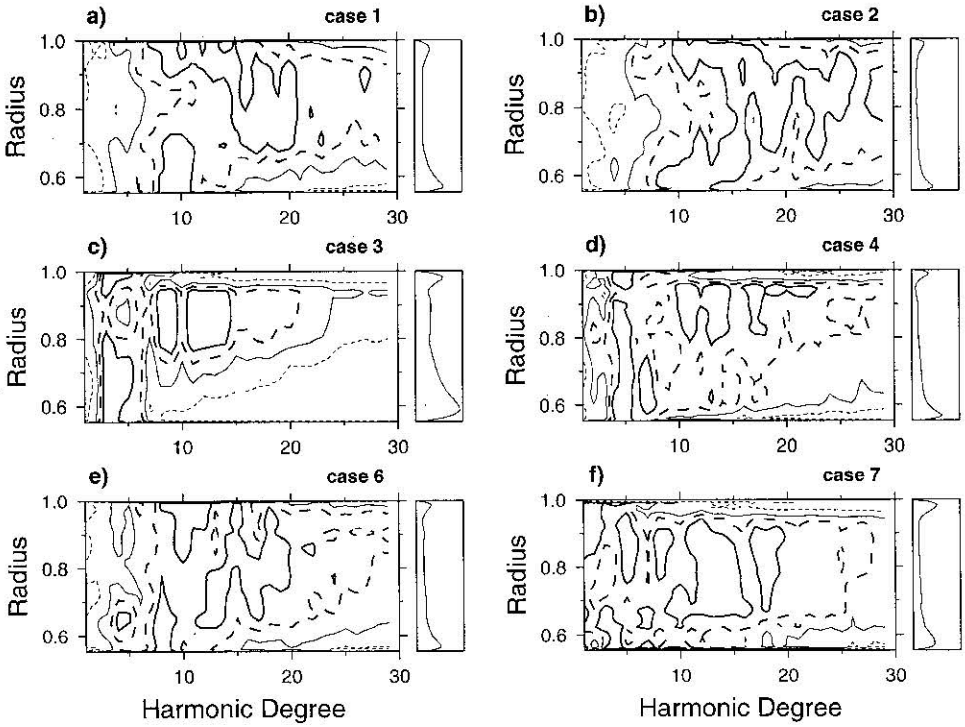

Figure 3. Radial dependence of normalized spectra for different cases. The left plots are the radial dependence of maximum power. Thin-dashed, thin solid, thick-dashed, and thick solid contours are for 0.2, 0.4, 0.6, and 0.8, respectively.

mantle (>670 km in depth) is a factor of 30 stronger than the upper mantle. Case 3 is identical to case 2, except that the lower mantle viscosity is increased by a factor of 30 (Table 4). Compared to case 2, the higher-viscosity lower mantle results in significantly longer wavelength structure with downwelling sheets extending to greater depths (Plate 1c). For case 3 with 74% internal heating, l=3 is the most significant wavelength throughout the mantle (Figure 3c), and this wavelength is much longer than that in case 2 (Figure 3b). The downwelling sheets extend to at least 1700 km depth, while the structure of upwellings is mainly cylindrical (Figures 2c and 2d).

The increased wavelength can be partially attributed to the effectively reduced *Ra* with increased viscosity within the lower mantle [*Bunge et al.*, 1996]. The reduced critical Rayleigh numbers for 2-D models with layered viscosity led *Bunge et al.* [1997] to suggest that other mechanisms may contribute to the longer wavelength flow. However, in the layered viscosity models by *Bunge et al.* [1996], the lower mantle viscosity was higher than the viscosity in isoviscous models. This may weaken the conclusion on the role of a weak upper mantle. Case 4 is identical to case 1 but has a factor of 30 weaker upper mantle. Although flow velocity in case 4 is dramatically increased compared with that in case 1 (Figure 4d), the thermal structure in case 4 has much longer wavelengths (Plate 1d and Figure 3d). Calculations in cases 1 and 4, therefore, provide a direct confirmation on the role of a weak upper mantle in forming the long-wavelength structure.

The layered viscosity structure also has important effects on the TBL thickness and averaged temperature profiles. For both cases 3 and 4, V_h is smaller near the bottom TBL than near the top TBL (Figure 4d). This leads to a thicker TBL at the bottom than that at the top (Figure 4c) and a colder mantle than isoviscous models (Figures 4a and 4c). It is interesting to notice that although case 3 has less vigorous convection and the same heat production rate as case 2, the mantle temperature in case 3 is smaller than that in case 2 (Figures 4a and 4c). This is different from constant viscosity models in which reduced convective vigor results in a hotter mantle if heat production rate is the same (e.g., cases 1 and 2 in Figure 4a). A weak upper mantle also introduces a strong subadiabatic temperature gradient in the lower mantle (Figure 4c).

3.3. Models With Temperature-Dependent Viscosity

Creep deformation of silicates is thermally activated, and the rheology of the mantle is expected to be strongly temperature-dependent. The influence of temperature-dependent viscosity is investigated with case 5 which includes a temperature-dependent rheology with E=6.9078 and A=1 (equation (10)), which leads to a factor of 10^3 variations in viscosity from T=0 to T=1. Ra=7.29x10^5, defined by the viscosity at T=0.5, is nearly an order of magnitude higher than that in *Ratcliff et al.* [1997]. Otherwise, case 5 is identical to case 2 with internal heating. Compared to the isoviscous model (case 2), the temperature-dependent rheology gives rise to thermal structure with a much longer wavelength (Plate 1e), consistent with previous studies [*Ratcliff et al.*, 1996, 1997; *Tackley*, 1996]. While the upwelling structure remains plume-like, the plumes are smaller in radius and have larger heads near the surface (Plate 1e and Figure 2d) compared to isoviscous models (Plate 1b). At a relatively shallow depth, there are significant variations in temperature along the strike of the linear downwelling structure, and the linear structure

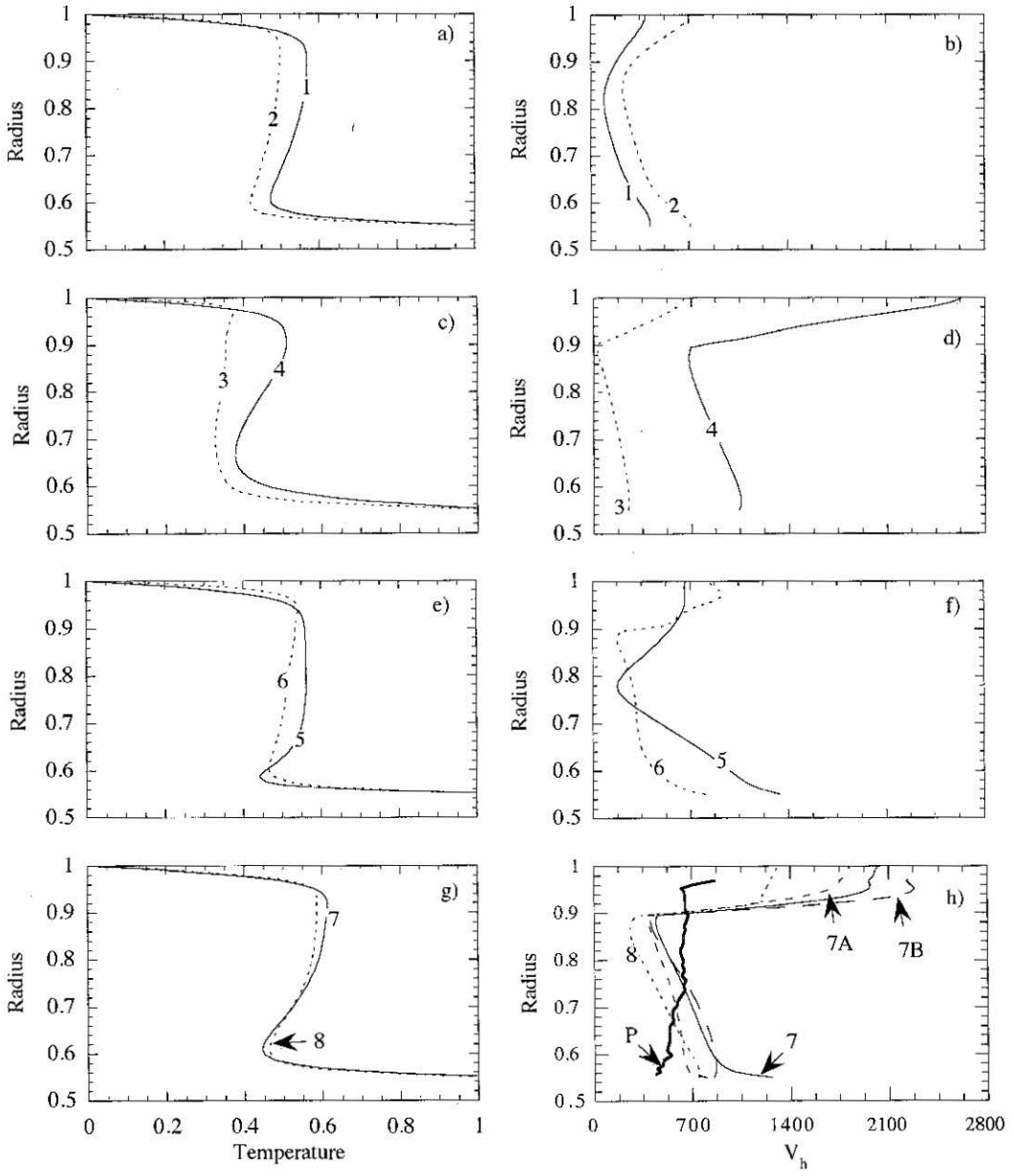

Figure 4. Radial dependence of azimuthally averaged temperature (Figures 4a, 4c, 4e, and 4g) and horizontal velocity (Figures 4b, 4d, 4f, and 4h) for cases 1-8 (case numbers are labelled). In Figure 4h the line labelled with P is the average horizontal velocity for upwelling plumes from t=9.25x10^{-4} to t=1.263x10^{-3}; the lines labelled with 7A and 7B are for the two calculations without buoyancy for upwellings and with constant viscosity in the lower mantle, respectively.

becomes disintegrated at great depths (Plate 1e and Figures 5 and 2c). A_r for downwellings is maximum at r=0.92 (i.e., 500 km depth) (Figure 2c), because the downwellings are wider at shallow depths (Figure 5).

The average horizontal velocity V_h at the bottom boundary is about twice the value at the surface (Figure 4f), a consequence of temperature-dependent viscosity that reduces the viscosity in the bottom TBL. This results in a thinner bottom TBL than the top TBL (Figure 4e). Compared to case 2, bottom heat flux increases, but surface heat flux remains about the same (Table 4). This leads to the higher average mantle temperature (Figures 4e and 4a) and lower internal heating rate in case 5 (Table 4). Case 5 has similar V_h near the surface to case 2 (Figures 4f and 4b), indicating a relatively mobile surface. The long-wavelength structure and the relative large surface V_h are characteristic of the sluggish convection regime with moderate viscosity variations [*Tackley*, 1996; *Ratcliff et al.*, 1997].

As either a temperature-dependent viscosity or a layered viscosity with a weak upper mantle can produce long-wavelength structure, it is interesting to investigate how the combination of temperature-dependent viscosity and layered viscosity influences the thermal structure. Case 6 is identical to case 4 with layered viscosity except that temperature-dependent viscosity with E=6.9078 is also included. The combination of layered and temperature-dependent viscosities

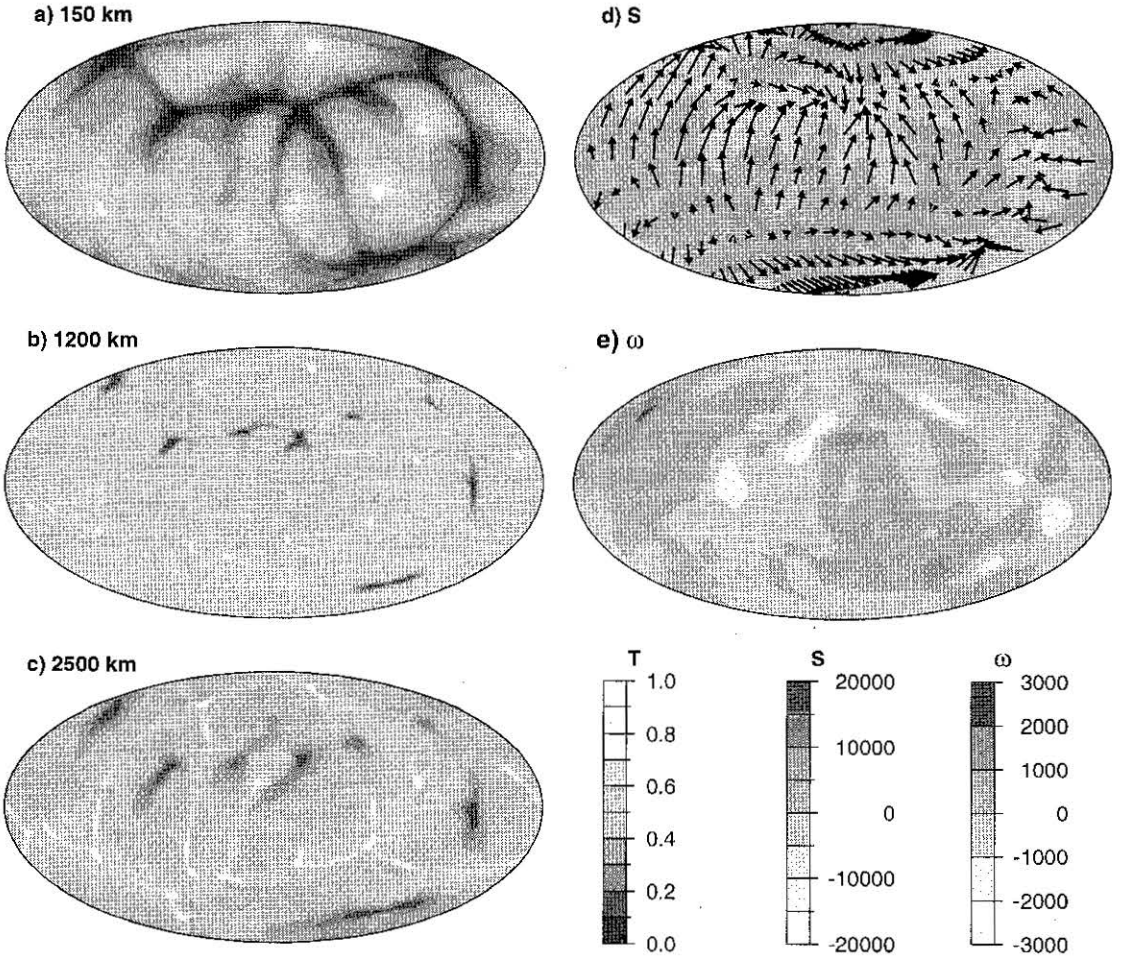

Figure 5. The temperature fields at three different depths (Figures 5a, 5b, and 5c), surface velocity and its divergence S, and radial vorticity ω (Figures 5d and 5 e) for case 5.

significantly reduces the dominant wavelength (Plate 1f and Figure 3e), compared with that from the layered viscosity model (Plate 1d and Figure 3d), indicating the important influence of temperature-dependent viscosity. Similar results were also reported based on 3-D Cartesian models at a smaller *Ra* [*Tackley*, 1996]. For case 6 the high viscosity at the shallow depths reduces the convective vigor significantly compared with case 4 (Figure 4f).

Temperature-dependent viscosity produces toroidal motion or radial vorticity at the surface (Figure 5e for case 5). However, the amplitude of vorticity is < 20% of the convergence (Figure 5d). This is significantly less than that in observed plate motion [*Hager and O'Connell*, 1978]. In addition, the surface motion is diffuse (Figure 5d) and significantly different from piecewise constant angular velocity observed for tectonic plates. This is consistent with previous findings based on 3-D Cartesian models that temperature-dependent rheology alone cannot produce plate-like surface motions [*Christensen and Harder*, 1991].

3.4. Models With Plates and Variable Viscosity

The combination of plates and layered viscosity has a dramatic influence on the flow, as we will demonstrate with cases 7 and 8. For the rheology used in case 7, E=9.2025, which gives rise to 10^4 viscosity variations due to temperature variations; preexponential constants A are 3, 0.05, and 3 in the top 120 km, the upper mantle, and lower mantle, respectively. *Ra* defined by the viscosity in the lower mantle at T=0.5 is 2.43×10^5 (Ra=2.43×10^7 if defined by viscosity at the CMB). For this case, average surface velocity is ~ 1 cm/yr, indicating that our *Ra* is still at least one order magnitude smaller than the Earth. The nondimensional heat production rate is 60 throughout the mantle, and internal heating rate is ~ 61% (Table 4). Initial temperature increases linearly from zero at the surface to 0.55 (i.e., average mantle temperature in case 5) at a depth of 120 km; T= 0.55 from 120 km depth to 250 km above the CMB, except within cold slabs; in the bottom 250 km the temperature increases from 0.55 to 1.0 at the CMB. Initially, cold slabs with T=0.47 are placed at depths from 120 to 400 km in current subduction zones.

We have integrated this model for more than seven transit times. The distribution of subduction zones becomes very different from the initial distribution with new downwellings developed at plate margins that are previously of other types, and upwellings also develop as the bottom thermal boundary layer becomes unstable (Plate 2 and Figure 6). The combination of a strongly temperature-dependent viscosity and weak plate margins gives rise to "plate-like" surface motion with localized divergence and vorticity at plate

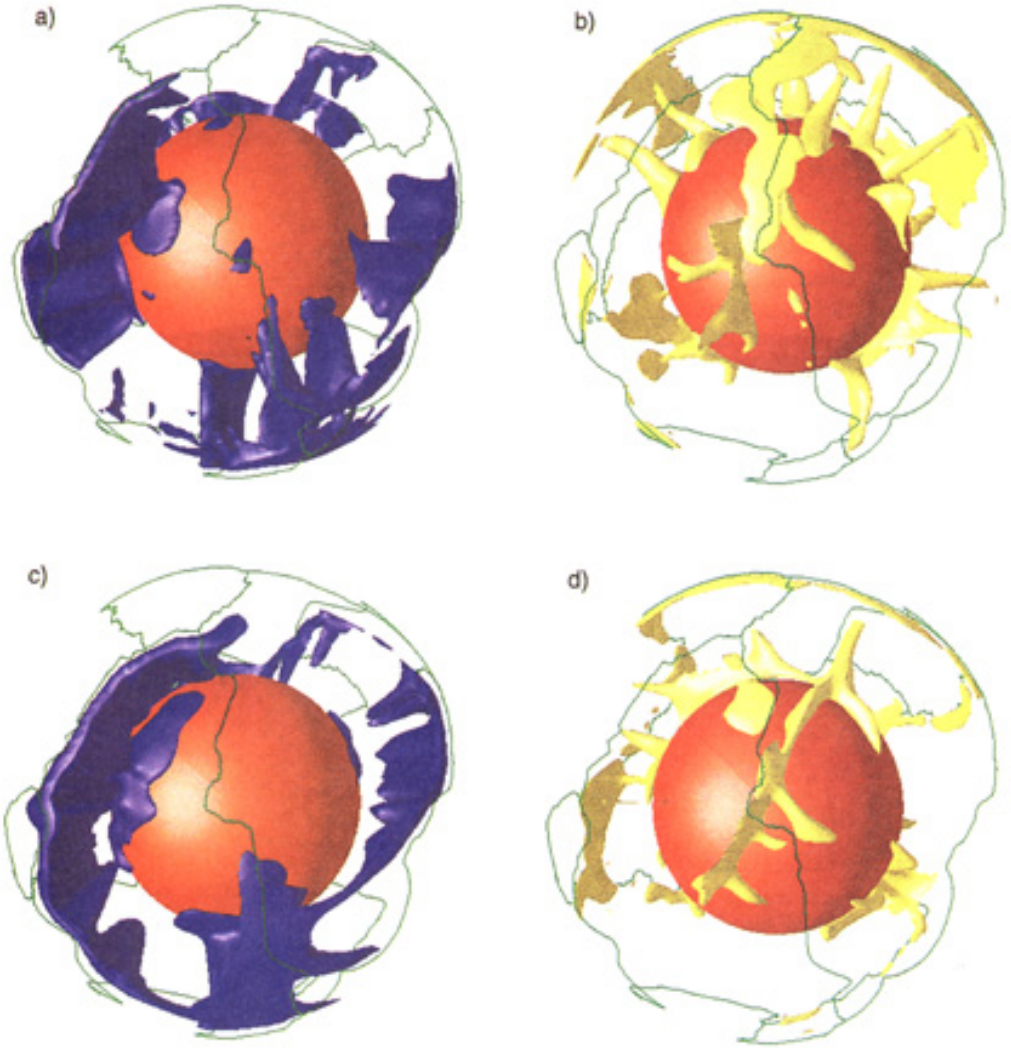

Plate 2. Isosurfaces of residual temperature for case 7 at t=9.25x10^{-4} (Plates 2a and 2b) and case 8 at t=1.187x10^{-3} (Plates 2c and 2d) with weak plate margins (green lines). The yellow and blue isosurfaces are for δT=0.15 and δT=-0.15, respectively.

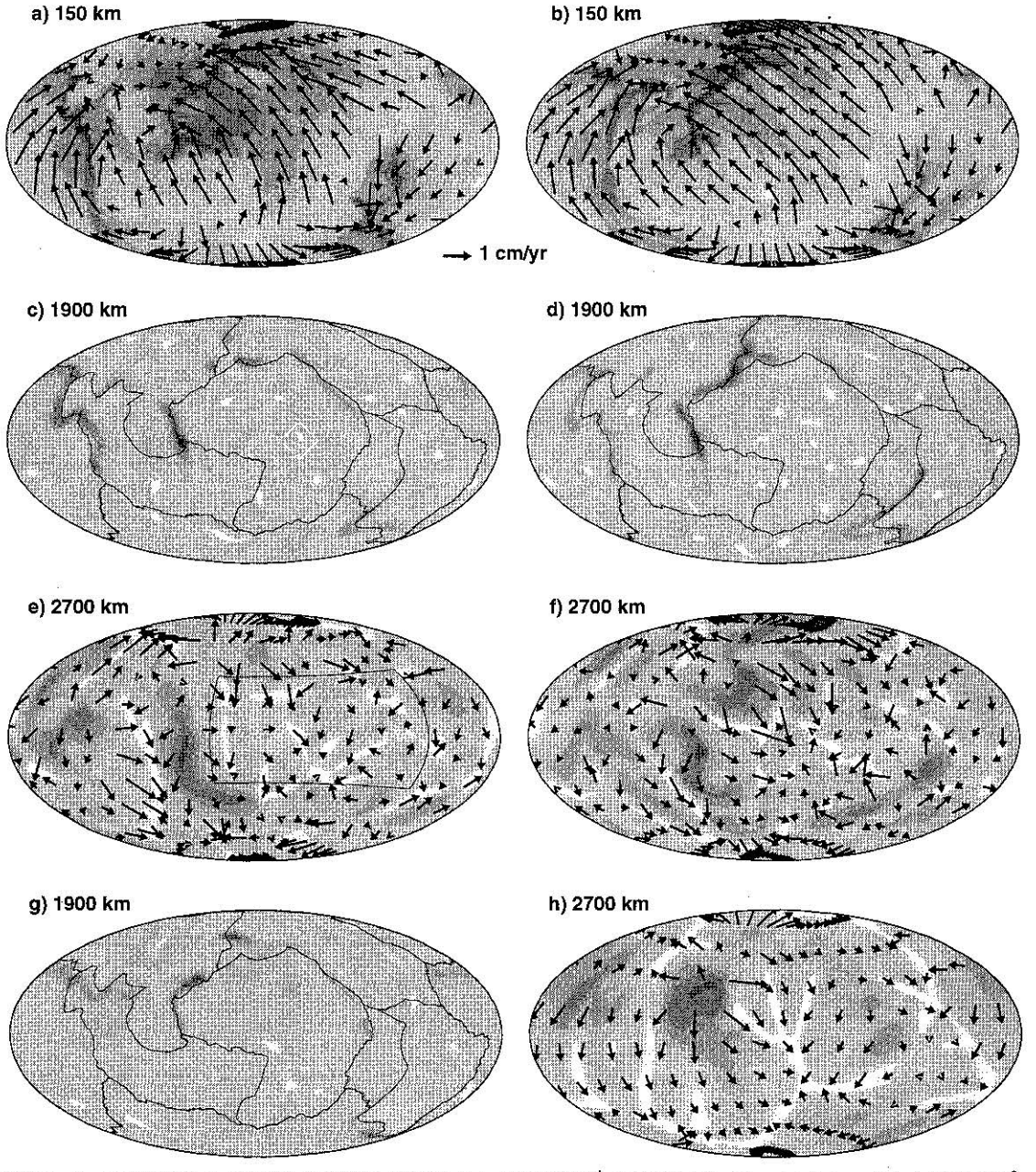

Figure 6. Temperature at three different depths at t=9.245x10^{-4} (Figures 6a, 6c, and 6e) and t=1.263x10^{-3} (Figures 6b, 6d, and 6f) for case 7 and at two different depths at t=1.187x10^{-3} (Figures 6g and 6h) for case 8. Flow velocities at the surface (Figures 2a and 2b) and CMB (Figures 2e, 2f, and 2h) are also plotted with the same scale. Plate boundaries are plotted in Figures 6c, 6d, and 6g.

margins (Figures 6a, 6b, 7a, and 7b). There is as much power in the divergence as in the vorticity in the surface motion, and many plate margins have a mixture of vorticity and divergence, both of which are consistent with observed plate motion. The "plate-like" motion has an important influence on the thermal structure within the mantle, as demonstrated in previous two-dimensional models [e.g., *Davies*, 1989; *Zhong and Gurnis*, 1994]. Our focus will be on general characteristics of thermal and flow structure and their relationship to surface plates.

Although time-dependent, the thermal structure in case 7 (Plate 2a and 2b at t=9.245x10^{-4}) has the following characteristics. With surface plates the thermal structure is predominated by long wavelengths directly related to the scales of plates (Figure 3f and Plate 2). The downwellings have linear structure initiating at the prescribed weak plate margins and extending to great depths in the mantle (Plate 2a and Figures 6a-6f). The upwellings originate at the CMB and have a plume-like structure throughout the mantle. There are also thermal anomalies associated with divergent plate boundaries (i.e., spreading centers), but these anomalies only exist at shallow depths (<200 km) (Plate 2b and Figures 6a, 6b and 2f).

The structural aspect ratio A_r for downwellings is significantly greater than 1 throughout the mantle, but A_r decreases steadily with depth and is insensitive to the threshold used to identify the structure (Figure 2e). However,

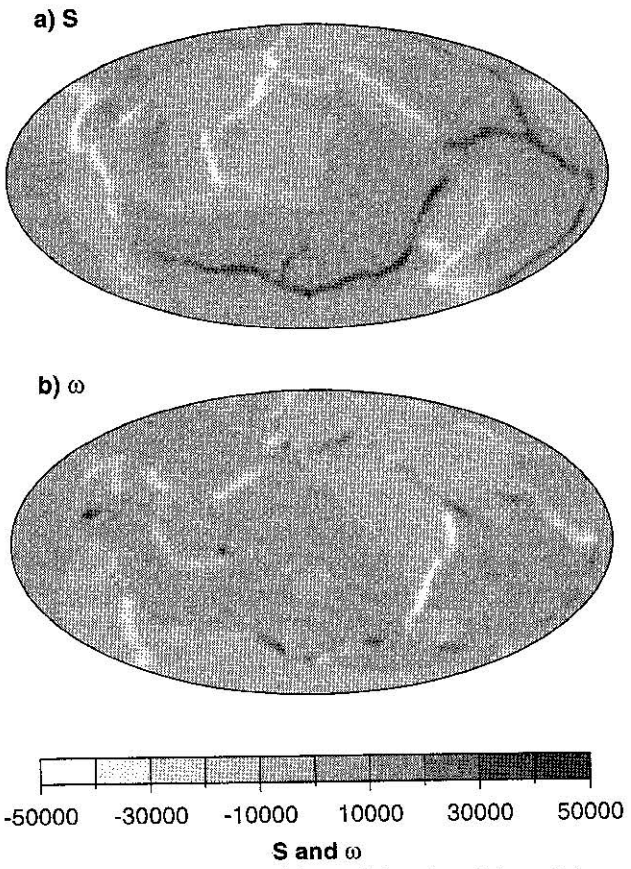

Figure 7. Divergence S (Figure 7a) and radial vorticity ω (Figure 7b) for surface velocity at t=9.25x10^{-4} in Case 7.

the decrease in A_r with depth is primarily caused by the increased width of downwellings because the average length L for downwellings actually increases slightly with depth except in the upper mantle (Figure 2g). The linear downwellings in the mantle display a similar along-strike morphologic structure to that of plate margins (Figures 6c and 6d), showing that plate margins control the downwelling structure. These coherent linear downwellings are significantly different from that found in all previous cases without plates in which the linear downwellings disintegrate at great depths (Figures 2a and 2c).

A_r for upwellings is close to unity except near the surface and CMB (Figure 2f), and the large A_r near the surface and CMB results from the linear structure for spreading centers at the surface (e.g., Plate 2b) and linear upwelling structure near the CMB (Figures 6e and 6f). Upwelling plumes can form under either plate margins or plate interiors, particularly for large plates like the Pacific (Plate 2 and Figures 6c and 6d). The upwelling plumes form between cold regions at CMB (Figures 6e and 6f). As they ascend to the surface, the upwelling plumes may become tilted if they are beneath plate interiors owing to the shearing of global and plate-scale mantle flow, particularly in the upper mantle where flow velocity is large owing to the small viscosity (Plate 2 and Figure 4h).

From t=9.245x10^{-4} to t=1.263x10^{-3}, there is a significant change in morphology and locations of downwellings and upwellings (Figures 6a-6f). During this period, new plumes form, while other plumes fade away. While the surface plate (e.g., the Pacific) travels over a distance of ~ 6000 km, the upwelling plumes have relatively small lateral motion (Figures 6c and 6d), although the average flow velocity at the CMB is almost 70% of that at the surface (Figure 4h). We have tracked the lateral motion for upwelling plumes at different depths from t=9.245x10^{-4} to t=1.263x10^{-3} (Figures 8a-8c). The upwelling plumes show quite coherent lateral motion at depths from 800 to 2370 km (Figures 8a-8c). The average horizontal velocity for the upwelling plumes V_h^p tends to decrease with the depth, which is opposite to the average horizontal velocity in the lower mantle (Figure 4h). Near the CMB, V_h^p is about one fifth of the surface plate motion and one third of the average velocity of CMB (Figure 4h). However, at the relatively shallow depths, V_h^p is nearly one third of surface plate motion (Figure 4h). There is a significant variability in the behaviors of mantle plumes. From t=9.245x10^{-4} to t=1.263x10^{-3}, some plumes (e.g., P2 in Figure 8a) are nearly stationary even if they are under fast moving plates, while others (e.g., P3 in Figure 8a) may display considerable motion.

In order to better understand the formation and motion of upwelling plumes, we re-solve flow field (equations (6) and (7)) at t=9.245x10^{-4} with the same thermal structure but excluding the hotter-than-average structure in the lower mantle (i.e., > 670 km depth). The surface motion from this calculation (7A) without upwelling plumes is similar to that from case 7 except the amplitude is slightly reduced by ~ 10% (Figures 6a and 9a), but the reduction in velocity at the CMB is much larger (Figures 4h, 6e and 9b). This indicates that the buoyancy of downwellings controls the surface motion, while the upwelling plumes contribute significantly to the motion at the CMB. The gross flow structure that diverges from cold regions at the CMB from calculation 7A is quite similar to that in case 7 (Figures 6e and 9b). Many upwelling plumes in case 7 tend to form in regions with relatively small horizontal velocities (or stagnant points) in calculation 7A (Figures 9c and 9d). To first order the buoyancy for upwellings does not significantly influence the horizontal motion in the vicinity of upwellings (Figures 9c-9f). However, the plume buoyancy may substantially alter the horizontal and vertical velocities within plumes (Figures 9e and 9f), and such plume-induced motion may stabilize the plumes. This may explain why the average horizontal motion of upwelling plumes decreases with the depth and becomes relatively stationary near the CMB (Figure 4h). This may also explain why some plumes are stationary over a long time and are nearly vertical throughout the mantle (e.g., P2 in Figure 8a).

We also compute the flow field from the thermal structure at 9.245x10^{-4} in case 7 but with a constant viscosity in the lower mantle (i.e., the viscosity at T=0.5). The general flow pattern at the surface and CMB from this calculation 7B (Figure 9g) is quite similar to that in case 7 with temperature-dependent viscosity (Figure 9d). However, the amplitude of motion is increased near the surface and within much of the lower mantle except near the CMB where the absence of temperature-dependent viscosity reduces the motion (Figure 4h). Moreover, the vertical flow velocity for upwelling plumes is reduced by more than a factor of 4, compared with that in case 7 (Figures 9f and 9h), indicating the influence of temperature-dependent viscosity on the dynamics of plumes including their trajectory.

Finally, we present case 8 with the plates and layered viscosity structure but without temperature-dependent

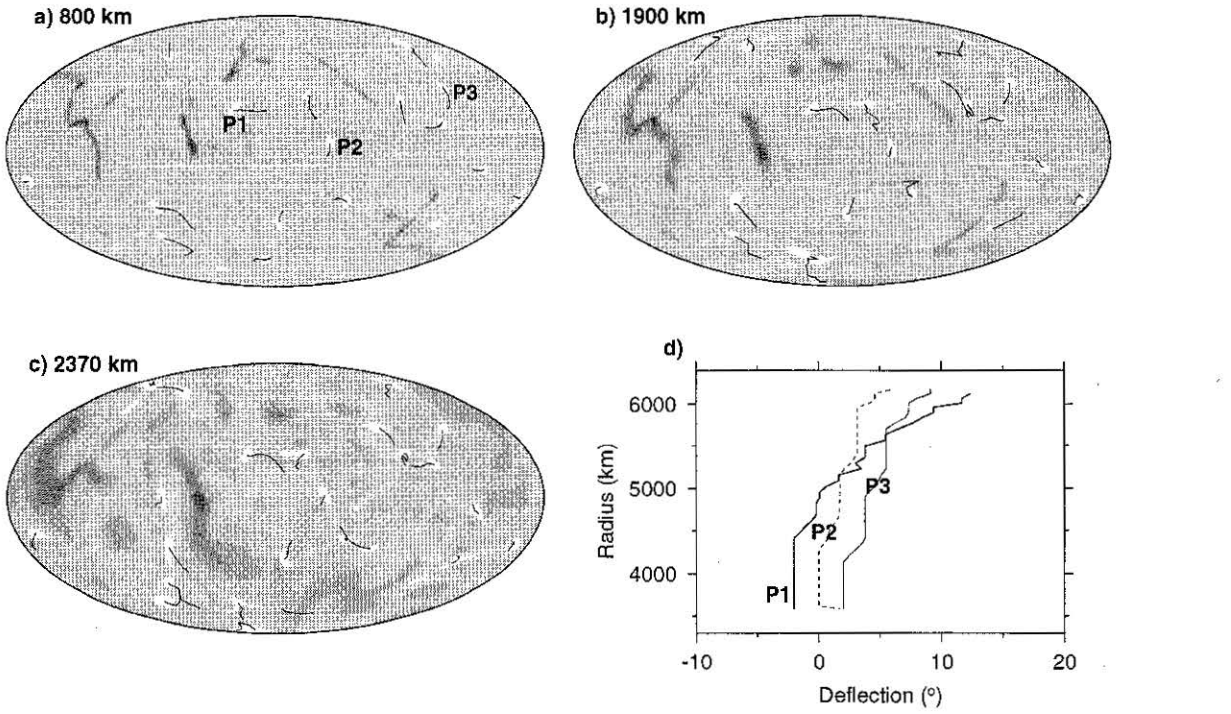

Figure 8. Thermal structure at t=9.245x10^{-4} for Case 7 at depths of 800 km (Figure 8a), 1900 km (Figure 8b), and 2370 km (Figure 8c) and the locations of upwelling plumes at these depths from t=9.245x10^{-4} to t=1.263x10^{-3}. Figure 8d shows the trajectory for three upwelling plumes that are labelled in Figure 8a.

viscosity. In this case the viscosities are 30, 0.1, 0.0333, and 2 in the top 120 km, weak zones, the upper mantle, and lower mantle, respectively. *Ra* defined by the viscosity in the lower mantle is 4x10^5. For Case 8, the average flow velocity is reduced by ~ 30% compared with that in case 7 with temperature-dependent viscosity (Figure 4h). There are two important changes in the thermal structure compared to case 7. The number of upwelling plumes is reduced significantly; the linear downwelling structure becomes disintegrated at the mid-mantle depths (Plates 2c and 2d and Figures 6g, 6h, and 2e). Although the convection is less vigorous (Figure 4h), because the downwellings have the same strength as the background mantle, linear downwellings have a greater tendency to disintegrate compared to the model with temperature-dependent viscosity.

4. Discussions

Understanding the origin of the long wavelengths observed in seismic tomography [e.g., *Su and Dziewonski*, 1992; *van der Hilst et al.*, 1997; *Masters et al.*, 1996] has been a goal in geodynamics. Long-wavelength thermal structure can be produced with a layered viscosity structure with a weak upper mantle [*Zhang and Yuen*, 1995; *Bunge et al.*, 1996, 1997], moderately temperature-dependent viscosity [*Tackley*, 1996; *Ratcliff et al.*, 1997], surface plates [*Davies*, 1988], and endothermic phase changes [*Tackley et al.*, 1993; *Tackley*, 1996]. We have examined the first three scenarios.

A temperature-dependent rheology with viscosity variations of 10^3 at Ra=7.29x10^5 (defined by the viscosity at T=0.5) results in significantly longer wavelength (Plate 1e), consistent with spherical models at smaller *Ra* [*Ratcliff et al.*, 1996, 1997] and Cartesian models [*Tackley*, 1996]. Comparison of our model with those of *Ratcliff et al.* [1996] suggests that the increase in wavelengths due to a temperature-dependent viscosity does not strongly depend on *Ra*. Layered viscosity structure leads to longer wavelengths (Plate 1d and Figure 3d) [*Zhang and Yuen*, 1995; *Bunge et al.*, 1996, 1997]. However, this increase in wavelengths due to the layered viscosity structure becomes less significant when temperature-dependent viscosity is included (Plate 1f and Figure 3e). *Tackley* [1996] found a similar trend in Cartesian models at smaller *Ra*. This may be because temperature-dependent viscosity gives rise to large viscosities at shallow depths that offset the "lubrication" of a weak upper mantle in layered viscosity models. This clearly demonstrates the sensitivity of thermal structure on mantle rheology, particularly the temperature-dependent viscosity.

Although with moderately temperature-dependent viscosity, convection models produce long-wavelength structures, temperature-dependent viscosity models are limited in two important respects. First, the models cannot produce "plate-like" surface motion (Figures 5d and 5e). Second, if a realistic activation energy is used, the large viscosity variation results in stagnant lid convection with dramatically reduced wavelengths of internal convection, as demonstrated by *Ratcliff et al.* [1997] and in Cartesian models by *Christensen* [1984], *Tackley* [1993], and *Moresi and Solomatov* [1995]. Of course, the extremely large viscosity at shallow depths for the Earth may be irrelevant because deformation at shallow depths is accommodated through other mechanisms such as faulting. Effective viscosity may be used to approximate faulting deformation. In our models with prescribed weak plate margins, "plate-like" surface motion and long-wavelength structure are produced (Plate 2 and Figure 7).

We have investigated the morphology of downwellings and

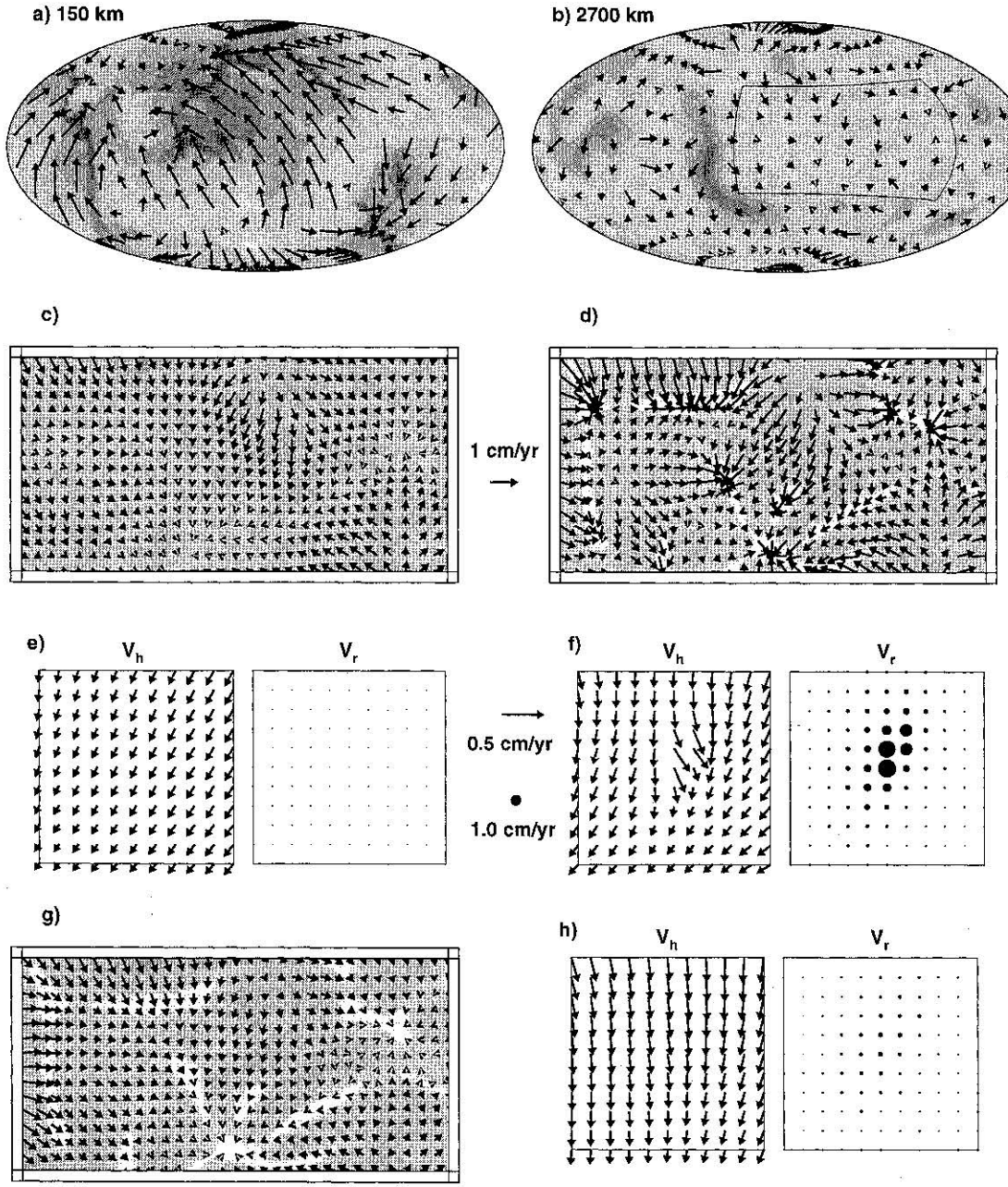

Figure 9. Flow velocity at the surface (Figure 9a) and CMB (Figure 9b) for calculation 7A. Also plotted in Figures 9a and 9b are the thermal structure at two different depths. Figures 9c and 9d are the horizontal velocity at CMB and thermal structure at a depth of 2700 km for regions outlined in Figures 9b (calculation 7A) and 6e (case 7), respectively. Figures 9e and 9f are for horizontal (V_h) and radial (V_r) velocities at a depth of 1900 km for a region surrounding a upwelling plume (see outline in Figure 6c) for calculation 7A and case 7, respectively. Figures 9g and 9h show the horizontal velocity at CMB for the same regions outlined in Figure 6e, and horizontal (V_h) and radial (V_r) velocities at a depth of 1900 km for a region surrounding a upwelling plume (see outline in Figure 6c) for calculation 7B. In Figures 9a and 9b, velocities have the same scale as in Figure 6.

upwellings in the mantle. In isoviscous models, cold downwellings form linear structure only at shallow depths, and they break into plume-like structure at great depths. The depth at which the linear structure breaks down depends on the vigor of convection or *Ra* and is shallower for larger *Ra* (Plates 1a and 1b and Figure 2a). The upwelling structure is symmetric to the downwellings in that the linear upwelling structure near the CMB turns into plume-like structure as the hot fluid ascends (Plates 1a and 1b and Figures 2a and 2b). Similar structural changes for upwellings and downwellings are also observed in temperature-dependent viscosity models, although cold downwellings owing to their high viscosity, can be maintained over a longer distance than the linear upwellings (Plate 1e and Figures 2c and 2d). These models show that in the absence of surface plates the dominant structure in the mantle away from thermal boundary layers is plume-like.

At low *Ra*, downwelling and upwelling structures are asymmetric with plume-like upwellings and linear sheet downwellings [*Bercovici et al.*, 1989], similar to case 3 (Plate 1c). The upwellings and downwellings with these structures are mutually compatible. The asymmetry has been attributed to the spherical shell geometry (i.e., smaller surface area at smaller radius) [*Bercovici et al.*, 1989]. However, the asymmetry can only be attained at low *Ra*, and at high *Ra* the symmetry to some extent is recovered (Plates 1a and 1b and Figures 2a and 2b). This is because at high *Ra* the vigor of convection tends to homogenize the thermal structure and the long linear sheet downwelling structure may give way to plume-like structure in order to more efficiently transfer the heat. When cold downwelling plumes reach the CMB, they push aside hot fluids. The hot fluids merge and, in many cases, form a linear structure at the CMB. This recovery of symmetry at relatively high *Ra* can also be seen in the spherical models by *Tackley et al.* [1993]. The change in downwelling structure is also consistent with previous studies with smaller *Ra* [*Glatzimaier et al.*, 1990; *Ratcliff et al.*, 1997] and 3-D Cartesian models with higher *Ra* [*Parmentier et al.*, 1994].

In models with relatively realistic rheological structure (i.e., surface plates and layered and temperature-dependent viscosity) the dominant structure for upwellings is plume-like, similar to models without plates (Plate 2 and Figure 2f). There are also linear thermal anomalies along the spreading centers, a consequence of "plate-like" surface motion, and these thermal anomalies cannot be traced down to 200 km depth (Plate 2 and Figure 2f). The downwellings show stronger linearity and extend into a great depth in the mantle, mainly due to the prescribed weak plate margins that facilitate the subduction with linear structure (Plate 2). Whether the linear downwelling structure can be maintained throughout the mantle while they descend may depend on mantle rheology. In models with temperature-dependent viscosity, the strengthened linear downwellings can largely maintain their structure throughout the mantle (Plate 2 and Figures 2e and 2g), although it is unclear how this result will be influenced by increased *Ra*, which tends to homogenize the structure.

Thermal structure from our models with plates explains well the seismic observations, including the shallow anomalies associated with spreading centers [*Zhang and Tanimoto*, 1992; *Masters et al.*, 1996], plume structure beneath hotspots [e.g., *Wolfe et al.*, 1997], and the linear structure beneath subduction zones that extends at least to the depth of mid-mantle [*van der Hilst et al.*, 1997; *Grand et al.*, 1997]. Recent seismic tomography studies show that linear downwellings appear to become disintegrated at the great depths (>1800 km) [*van der Hilst and Karason*, 1999]. It has also been suggested that subducted slabs can keep the morphology that they acquire at trenches for quite a long time as they descend into the lower mantle [*van der Voo et al.*, 1999]. Interpretation of seismic images may hinge on our understanding of the effects of rheology and composition of the mantle on the mantle structure [*Kellogg et al.*, 1999].

Our dynamic models with plates also demonstrate that surface motion is mainly determined by buoyancy force associated with downwellings (Figures 6a and 9a). This is because plate-scale flow associated with subduction of top thermal boundary layer transfers most of the heat out of the mantle, whereas the heat transfer associated with upwelling plumes is secondary, a fundamental feature for the Earth dynamic system [*Davies*, 1988; *Davies and Richards*, 1992] that is captured in our models. This result also supports the instantaneous flow models for plate motion in which only subducted slabs are included as driving forces [*Lithgow-Bertolloni and Richards*, 1998].

By controlling surface plate motion and global flow field, buoyancy for downwellings to first order determines where upwelling plumes form at the CMB. Upwelling plumes tend to form at the stagnant points predicted from the buoyancy of downwellings, and these stagnant points are often located between downwellings (Figures 6e, 9b-9d). As a result, upwelling plumes can form under spreading centers or plate interiors, particularly for large plates like the Pacific (e.g., Figure 6c). This may explain the apparent anticorrelation between distribution of hotspots and fast seismic wave speed anomalies in the lower mantle [*Richards et al.*, 1988; *Steinberger and O'Connell*, 1998] if these fast anomalies represent cold downwellings. The horizontal motion in the vicinity of the upwellings is not very sensitive to the buoyancy of upwellings (Figures 9e and 9f). Therefore the horizontal migration of upwellings to first order is influenced by mantle flow determined by the slab buoyancy, as suggested by *Steinberger and O'Connell* [1998].

However, we have also observed plumes that in spite of under fast moving plates appear insensitive to global flow and can stay stationary in the mantle over a long time (e.g., P2 in Figure 8a), possibly because these plumes can produce significant localized flow to reduce the influence of the global flow. For well-established upwelling plumes the combination of temperature-dependent viscosity and high plume temperature may yield vertical plume velocity that is much larger than the plate motion (Figure 9f). The vertical velocity of upwelling plumes can be greatly enhanced with the coupling of viscous heating and temperature-dependent viscosity [*Larson and Yuen*, 1997]. The formation of plumes at stagnant points on the CMB and the possibly strong localized flow induced by plume buoyancy, temperature-dependent rheology, and viscous heating may contribute to the observed stationarity between hotspots, although the high viscosity lower mantle may also play a role [*Steinberger and O'Connell*, 1998]. Clearly, more studies that include large-scale plate motion, realistic rheology, and plume buoyancy are needed in order to understand the plume dynamics better.

It should be pointed out that our models with plates have two unrealistic aspects: symmetric subduction and prescribed weak plate margins. Asymmetric subduction or one-sided subduction observed for the Earth may be due to the thrust faults that are not considered yet in our models. This should be considered in the future, as in Cartesian models [*Zhong et al.*, 1998]. The migration of plate margins, especially for converging margins, may be important for the dynamics of subducted slabs [*Gurnis and Hager*, 1988; *Kincaid and Olson*, 1987; *Zhong and Gurnis*, 1995]. However, the motion of converging margins is typically smaller than the motion of plates [*Jarrard*, 1986]. We believe that it will not significantly change our main results. In addition, the radii of upwelling plumes in our models are large because the models use relatively small Rayleigh numbers. High-resolution models at higher *Ra* with a better physical treatment of plate margins and possibly different compositions may be needed to examine how linear downwelling structure evolves with depths and how upwelling plumes are influenced by downwellings and surface plate motion. Future models also need to consider the effects of compressibilty, which may also increase the

wavelengths of mantle structure, as demonstrated in 3-D Cartesian models [e.g., *Tackley*, 1996].

5. Conclusions

We have investigated how the mantle thermal structures including both the scales and morphology depend on heating modes, vigor of convection, and viscosity structure including layered viscosity, temperature-dependent viscosity, and surface plates in 3-D spherical models of mantle convection. We find that in the absence of surface plates either a layered viscosity with a weak upper mantle or temperature-dependent viscosity with moderately large activation energy can produce long-wavelength structures in the mantle, consistent with previous studies with temperature-dependent viscosity [*Tackley*, 1996] and layered viscosity models [*Zhang and Yuen*, 1995; *Bunge et al.*, 1996]. However, combining the layered viscosity structure with a temperature-dependent viscosity results in structure with significantly shorter wavelengths. Our models confirm that the dominant wavelength of thermal structure within the mantle is mainly controlled by the surface plates [*Davies*, 1988].

Our models with significant internal heating, layered and temperature-dependent viscosity, and surface plates explain to first order the structure revealed from seismic tomography. Our models show that hot upwellings initiate at core-mantle boundary (CMB) with linear structures, and as they ascend, the linear upwellings change into quasi-cylindrical plumes. Linear upwelling structures are generated at shallow depths (<200 km) in the vicinity of diverging plate margins due to surface plate motion. Linear sheets are the predominant structure for cold downwellings that originate at converging plate margins. The evolution of linear downwellings as they descend may depend on the rheology of the mantle. A temperature-dependent viscosity strengthens the cold downwellings and therefore helps maintain linear downwelling structure in the mantle.

Our models also show that downwellings control not only surface plate motions but also the locations of upwellings. Upwellings tend to form at stagnation points on the CMB predicted solely from the buoyancy forces of downwellings, which causes the horizontal motion of upwelling plumes to decrease with depth. This explains the anticorrelation between hotspot distribution and fast seismic wave speed anomalies. Although downwellings to first order also determine the horizontal motion of upwelling plumes, plumes may produce significant localized flow to reduce the influence of global flow on their trajectories. With the tendency of the plume formation in stagnation regions on the CMB this may also have important implications to the observed stationarity of hotspots.

Appendix A: Spherical Finite Element Analyses for the Stokes' Flow

A Galerkin formulation for incompressible Stokes' flow (i.e., equations (6) and (7)) can be written as [*Hughes*, 1987]

$$\int q u_{i,i} dV = 0, \tag{A1}$$

$$\int w_{i,j} \eta u_{i,j} dV - \int w_{i,j} P \delta_{ij} dV = \int \delta \rho g w_i \delta_{ir} dV + \int w_i h_i dS, \tag{A2}$$

where q and w_i are the interpolation functions for pressure and velocity, respectively.

Stiffness matrix is derived from the evaluation of strain energy [*Hughes*, 1987]

$$\int w_{i,j} \eta u_{i,j} dV = \int \varepsilon(\mathbf{w})^T D \varepsilon(\mathbf{u}) dV, \tag{A3}$$

where

$$\varepsilon(\boldsymbol{u}) = \begin{pmatrix} e_{\theta\theta} \\ e_{\varphi\varphi} \\ e_{rr} \\ e_{\theta\varphi} \\ e_{\theta r} \\ e_{\varphi r} \end{pmatrix} = \begin{pmatrix} \dfrac{\partial u_\theta}{r\partial\theta} + \dfrac{u_r}{r} \\ \dfrac{1}{r\sin\theta}\dfrac{\partial u_\varphi}{\partial\varphi} + \dfrac{u_\theta \cot\theta}{r} + \dfrac{u_r}{r} \\ \dfrac{\partial u_r}{\partial r} \\ \dfrac{1}{r\sin\theta}\dfrac{\partial u_\theta}{\partial\varphi} - \dfrac{u_\varphi \cot\theta}{r} + \dfrac{\partial u_\varphi}{r\partial\theta} \\ \dfrac{\partial u_\theta}{\partial r} - \dfrac{u_\theta}{r} + \dfrac{\partial u_r}{r\partial\theta} \\ \dfrac{1}{r\sin\theta}\dfrac{\partial u_r}{\partial\varphi} - \dfrac{u_\varphi}{r} + \dfrac{\partial u_\varphi}{\partial r} \end{pmatrix}, \tag{A4}$$

and D is a diagonal matrix with diagonal elements η(2, 2, 2, 1, 1, 1).

We use isoparametric elements, and the velocities in each element can be related to nodal velocities with shape function N_a

$$\begin{pmatrix} u_\theta \\ u_\varphi \\ u_r \end{pmatrix} = \sum_a N_a \begin{bmatrix} \boldsymbol{e}_\theta \cdot \boldsymbol{e}_\theta^a & \boldsymbol{e}_\theta \cdot \boldsymbol{e}_\varphi^a & \boldsymbol{e}_\theta \cdot \boldsymbol{e}_r^a \\ \boldsymbol{e}_\varphi \cdot \boldsymbol{e}_\theta^a & \boldsymbol{e}_\varphi \cdot \boldsymbol{e}_\varphi^a & \boldsymbol{e}_\varphi \cdot \boldsymbol{e}_r^a \\ \boldsymbol{e}_r \cdot \boldsymbol{e}_\theta^a & \boldsymbol{e}_r \cdot \boldsymbol{e}_\varphi^a & \boldsymbol{e}_r \cdot \boldsymbol{e}_r^a \end{bmatrix} \begin{pmatrix} u_\theta^a \\ u_\varphi^a \\ u_r^a \end{pmatrix} = \sum_a N_a C \begin{pmatrix} u_\theta^a \\ u_\varphi^a \\ u_r^a \end{pmatrix}, \tag{A5}$$

where $\boldsymbol{e}_i$ is the unit vector in i direction; the superscript a represents the nodal values; the matrix C is approximately a unit matrix for elements far away from the two poles, but the off-diagonal terms are significant for elements near the poles (i.e., θ=0 and π).

Substituting (A5) into (A4) leads to

$$\varepsilon(\boldsymbol{u}) = \sum_a B_{ij}^a u_j^a, \tag{A6}$$

where B matrix is a 6x3 matrix. The strain energy (A3) can be written as

$$\int \varepsilon(\boldsymbol{w})^T D \varepsilon(\boldsymbol{u}) dV = \sum_a w_j^a \sum_b \left(\int B_{ji}^a D_{il} B_{lm}^a dV \right) u_m^b. \tag{A7}$$

The elemental stiffness matrix for node a and b is a 3x3 matrix and can be expressed as

$$K = \int B_{ji}^a D_{il} B_{lm}^a dV. \tag{A8}$$

The pressure term involves $\int w_{i,i} P dV$. The divergence of velocity is

$$w_{i,i} = \frac{\partial w_r}{\partial r} + \frac{2w_r}{r} + \frac{\partial w_\theta}{r\partial\theta} + \frac{\cot\theta w_\theta}{r} + \frac{1}{r\sin\theta}\frac{\partial w_\varphi}{\partial\varphi}. \tag{A9}$$

Again using (A5), the divergence within an element can be expressed as

$$w_{i,i} = \sum_a (w_\theta^a, w_\varphi^a, w_r^a) \begin{pmatrix} G_1^a \\ G_2^a \\ G_3^a \end{pmatrix}. \tag{A10}$$

Therefore

$$\int w_{i,i} P dV = \sum_a (w_\theta^a, w_\varphi^a, w_r^a) \int \begin{pmatrix} G_1^a \\ G_2^a \\ G_3^a \end{pmatrix} P dV. \quad \text{(A11)}$$

The force term involves $\int \delta\rho g w_i \delta_{ir} dV$, and with (A5) it can be expressed as

$$\int \delta\rho g w_r dV = \sum_a w_i^a \int N_a C_{3i} \delta\rho g dV, \quad \text{(A12)}$$

where C_{3i} is the last row of C matrix in (A5).

Finally, after substituting (A7), (A11), and (A12), we have a matrix equation [*Hughes*, 1987; *Moresi and Gurnis*, 1996]

$$\begin{bmatrix} K & G \\ G^T & 0 \end{bmatrix} \begin{pmatrix} U \\ P \end{pmatrix} = \begin{pmatrix} F \\ 0 \end{pmatrix}. \quad \text{(A13)}$$

We use a two-level Uzawa algorithm to solve this matrix equation to obtain the velocity and pressure fields [*Moresi and Gurnis*, 1996].

Appendix B: A Full Multigrid Solver and Parallel Computing

In the original Cartesian Citcom, an efficient multigrid solver is used to solve the velocity field with a Uzawa algorithm [*Moresi and Gurnis*, 1996]. This code has been ported onto parallel computers with the standard Message Passing Interface, MPI [*Zhong et al.*, 1998]. CitcomS uses a very different design for numerical grids because of the spherical geometry (Figure 1), whose design was partially influenced by the mesh in another mantle convection code, Terra [*Baumgarder*, 1985]. Parallelism is naturally embedded for this type of numerical grid design [e.g., *Baumgarder*, 1985] because exchange of information is necessary between adjacent blocks in order to carry out the calculations even on a single-processor workstation.

In addition to parallel computing, CitcomS also implements the full multigrid algorithm [*Press et al.*, 1992] coupled with a consistent projection scheme. We also notice that a different full multigrid algorithm was developed for a Cartesian Citcom by *Moresi and Salamotov* [1998]. With the consistent projection scheme we consider the effects of volumes of elements on the smoothing projection from one level of grids to another, because the coefficients in matrix equations at different grid levels in the finite element method are directly scaled with the volume of elements. We have found that for Cartesian models with either temperature-dependent viscosity and isoviscous structure the full multigrid algorithm with the consistent projection scheme can lead to a speedup of at least a factor of 3 compared to the original Citcom. In implementing the full multigrid algorithm for CitcomS we treat each block of grids separately (e.g., $12x2^n x2^n x2^n$); consequently, special treatment for boundary nodes between each block is needed to ensure the convergence. We find that the Jacobi iteration for boundary nodes and Gauss-Seidel iteration for interior nodes work quite well.

Owing to different requirements for the parallel computing and the multigrid algorithm, merging them together has been quite challenging. An efficient multigrid algorithm requires calculations at not only fine but also coarse grids, while effective parallel computing prefers a computational domain that has a large ratio of volume to surface area. This means that parallel computing becomes less efficient for calculations at the coarse grid level. However, we find that parallel computing is always beneficial even for our full multigrid algorithm. Benchmarks and comparisons have proven that CitcomS combines together the accuracy, efficiency, and robustness and is a very useful tool for studying global geodynamic problems.

Appendix C: Definitions of Benchmark Problems

We will define the three benchmark problems. The benchmark results are presented in Tables 1 to 3 and are discussed in section 2.3. The first benchmark problem only tests the Stokes' flow in which equations (6) and (7) are solved. The inner radius $r_i = 0.55$, and the outer radius $r_o = 1$. The driving force is

$$T = \delta(r - \frac{r_i + r_o}{2}) Y_{lm}(\theta, \varphi), \quad \text{(C1)}$$

and $Ra = 1$. Free slip boundary conditions are applied on both surface and bottom boundaries. For this problem, propagator matrix techniques can be used to solve (6) and (7) analytically [e.g., *Hager and O'Connell*, 1981]. The numerical solutions are straightforward with the input T and Ra.

The second benchmark problem is on the determination of critical Rayleigh numbers. Critical Rayleigh numbers are the Rayleigh numbers at which the flow is unstable to thermal perturbations. For this problem, equations (6), (7), and (8) need to be solved. Critical Rayleigh numbers can be determined with linear stability analyses [*Chandrasekhar*, 1961]. Critical Rayleigh numbers at different spherical harmonic degrees have been given for bottom-heated isoviscous flows in a spherical shell with free-slip and isothermal boundary conditions at $r_i = 0.50$ and $r_o = 1$, and gravity that is linearly dependent on the radius. The critical Rayleigh numbers for each harmonic degree can also be determined from numerical solutions [e.g., *Zhong and Gurnis*, 1993].

The third benchmark problem concerns thermal convection with finite amplitude. For this problem, we will solve equations (6), (7), and (8) at Rayleigh numbers significantly larger than the critical Rayleigh numbers. Because no analytic solutions exist for this problem, we compare our results (Nussult numbers) from CitcomS with previously published results by *Bercovici et al.* [1989] and *Ratcliff et al.* [1996]. Two calculations at different Rayleigh numbers have been performed for bottom-heated isoviscous flows with free slip and isothermal boundary conditions at $r_i = 0.55$ and $r_o = 1$, and constant gravitational acceleration within the shell.

Acknowledgements: Computations were performed on a Cray T3E at GSFC of NASA and a HP Exemplar at CACR of Caltech. S.Z. started this project shortly before leaving Caltech. S.Z. would like to thank RSES at ANU for a visiting fellowship and CSIRO for arranging a visit to AGCRC. We thank Marc Parmentier, R. van der Hilst, and T. Ratcliff for discussions, B. H. Hager for reading the manuscript, and S. Solomatov, P. Tackley, and an anonymous reviewer for their reviews. This represents contribution 8630 of the Division of Geological and Planetary Sciences, Caltech.

References

Bathe, K.-J., *Finite Element Procedures*, Prentice Hall, Englewood Cliffs, N. J., 1995.

Baumgardner, J. R., Three dimensional treatment of convection flow in the Earth's mantle, *J. Stat. Phys., 39*, (5/6) 501-511, 1985.

Bercovici, D., Generation Of Plate-Tectonics From Lithosphere-Mantle Flow And Void-Volatile Self-Lubrication, *Earth Planet. Sci. Lett., 154*, 139-151, 1998.

Brooks, A. N., A Petrov-Galerkin Finite Element Formulation for Convection Dominated Flows, Ph. D. thesis, Cali. Inst. of Technol., Pasadena, 1981.

Bunge, H-P., M. A. Richards, C. Lithgow-Bertelloni, J. R. Baumgardner, and S. P. Grand, Time scales and heterogeneous structure in geodynamic Earth models, *Science, 280*, 91-95, 1998.

Bunge, H-P., M. A. Richards, and J. R. Baumgardner, Effect of depth-dependent viscosity on the planform of mantle convection, *Nature, 379*, 436-438, 1996.

Bunge, H-P., M. A. Richards, and J. R. Baumgardner, A sensitivity study of 3-dimensional spherical mantle convection at 10^8 Rayleigh number: effects of depth-dependent viscosity, heating mode, and an endothermic phase-change, *J. Geophys. Res., 102*, 11991-12007, 1997.

Chandrasekhar, S., *Hydrodynamic and Hydromagnetic Stability*, Dover, Publications Inc., N. Y., 1961.

Christensen, U., Heat transport by variable viscosity convection and implications for the Earth's thermal evolution, *Phys. Earth Planet. Inter., 35*, 264-282, 1984.

Christensen, U. R., and H. Harder, 3-D convection with variable viscosity, *Geophys. J. Int., 104*, 213-226, 1991.

Courtney R. C., and C. Beaumont, Thermally-activated creep and flexure of the oceanic lithosphere, *Nature, 305*, 201-204, 1983.

Davies, G. F., Mantle convection model with a dynamic plate: Topography, heat flow and gravity anomalies, *Geophys. J. Int., 98*, 461-464, 1989.

Davies, G. F., Role of the lithosphere in mantle convection, *J. Geophys. Res., 93*, 10451-10466, 1988.

Davies, G. F., and M. A. Richards, Mantle convection, *J. Geol., 100*, 151-206, 1992.

Fukao, Y., M. Obayashi, H. Inoue, and M. Nenbai, Subducting slabs stagnant in the mantle transition zone, *J. Geophys. Res., 97*, 4809-4822, 1992.

Forte, A. M. and W. R. Peltier, Plate tectonics and aspherical Earth structure: The importance of poloidal-toroidal coupling, *J. Geophys. Res., 92*, 3645-3679, 1987.

Glatzmaier, G. A., G. Schubert, and D. Bercovici, Chaotic, subduction-like downflows in a spherical models of convection in the Earth's mantle, *Nature, 347*, 274-277, 1990.

Grand, S. P., Mantle shear structure beneath the Americas and surrounding oceans, *J. Geophys. Res., 99*, 11591-11622, 1994.

Grand, S. P., R. D. ven der Hilst, and S. Widiyantoro, Global seismic tomography: A snapshot of convection in the Earth, *GSA Today, 7*, 1-7, 1997.

Gurnis, M., A reassessment of the heat transport by variable viscosity convection with plates and lids, *Geophys. Res. Lett., 16*, 179-182, 1989.

Gurnis, M., and B. H. Hager, Controls on the structure of subducted slabs, *Nature, 335*, 317-321, 1988.

Gurnis, M., S. Zhong, and J. Toth, On the competing roles of fault reactivation and brittle failure in generating plate tectonics from mantle convection, In Geophys. Monograph Ser., in press, AGU, Washington, D. C., 2000.

Hager, B. H., and R. J. O'Connell, A simple global model of plate dynamics and mantle convection, *J. Geophys. Res., 86*, 4843-4878, 1981.

Hager, B. H., and M. A. Richards, Long-wavelength variations in Earth's geoid: Physical models and dynamical implications, *Philos. Trans. R. Soc. London.*, Ser. A, *328*, 309-327, 1989.

Hager, B. H., and R. J. O'Connell, Kinematic models of large-scale flow in the Earth's mantle, *J. Geophys. Res., 84*, 1031-1048, 1979.

Hughes, T. J. R., *The Finite Element Method*, Prentice-Hall, Englewood Cliffs, N.J., 1987.

Jarrard, R. D., Relations among subduction parameters, *Rev. Geophys., 24*, 217-284, 1986.

Karato S, and P. Wu, Rheology of the upper mantle: A synthesis, *Science, 260*, 771-778, 1993.

Katzman, R., L. Zhao, T. H. Jordan, High-resolution, 2-dimensional vertical tomography of the central Pacific mantle using ScS reverberations and frequency-dependent travel-times, *J. Geophys. Res., 103*, 17933-17971, 1998.

Kellogg, L. H., B. H. Hager, and R. D. van der Hilst, Compositional stratification in the deep mantle, *Science, 283*, 1881-1884, 1999.

Kincaid C. and P. Olson, An experimental study of subduction and slab migration, *J. Geophys. Res., 92*, 13832-13840, 1987.

King, S. D. and B. H. Hager, The Relationship Between Plate Velocity and Trench Viscosity in Newtonian and Power-Law Subduction Calculations, *Geophys. R. Lett., 17*, 2409-2412, 1990.

King, S. D., A. Raefsky, and B. H. Hager, ConMan: Vectorizing a finite element code for incompressible two-dimensional convection in the Earth's mantle, *Phys. Earth Planet. Inter., 59*, 195-207, 1990.

Larson, T. B. and D. A. Yuen, Fast plumeheads - temperature-dependent versus non-Newtonian rheology, *Geophy. R. Lett., 24*, 1995-1998, 1997.

Lithgow-Bertelloni, C., and M. A. Richards, The dynamics of Cenozoic and Mesozoic plate motions, *Rev. Geophys., 36*, 27-78, 1998.

Masters, G., S. Johnson, G. Laske, and H. Bolton, A shear-velocity model of the mantle, *Philol. Trans. R. Soc. London, Ser. A, 354*, 1385-1410, 1996.

Mitrovica, J. X, and A. M. Forte, Radial profile of mantle viscosity: Results from the joint inversion of convection and postglacial rebound observables, *J. Geophys. Res., 102*, 2751-2769, 1997.

Moresi, L. and V. S. Solomatov, Mantle convection with a brittle lithosphere: Thoughts on the global tectonic styles of the Earth and Venus, *Geophys. J. Int., 133*, 669-682, 1998.

Moresi, L., and M. Gurnis, Constraints on the lateral strength of slabs from three-dimensional dynamic flow models, *Earth Planet. Sci. Lett., 138*, 15-28, 1996.

Moresi, L. and V. S. Solomatov, Numerical Investigation of 2d Convection with Extremely Large Viscosity Variations, *Phys. Fluids, 7*, 2154-2162, 1995.

Parmentier, E. M., C. Sotin, and B. J. Travis, Turbulent 3D thermal convection in an infinite Prandtl number, volumetrically heated fluid: implications for mantle dynamics, *Geophys. J. Int., 116*, 241-251, 1994.

Press, W. H., S. A. Teukolsky, W. T. Vetterling, B. P. Flannery, *Numerical Recipes*, 2nd ed., 963 pp., Cambridge Univ. Press, New York, 1992.

Puster, P., B. H. Hager, and T. H. Jordan, Mantle convection experiments with evolving plates, *Geophys. Res. Lett., 22*, 2223-2226, 1995.

Ramage, A., and A. J. Wathen, Iterative solution techniques for the Stokes and Navier-Stokes equations, *Int. J. Numer. Methods Fluids, 19*, 67-83, 1994.

Ratcliff, J. T., G. Schubert, and A. Zebib, Steady tetrahedral and cubic patterns of spherical-shell convection with temperature-dependent viscosity, *J. Geophys. Res., 101*, 25,473-25,484, 1996.

Ratcliff, J. T., P. J. Tackley, G. Schubert, and A. Zebib, Transitions in thermal-convection with strongly variable viscosity, *Phys. Earth Planet. Inter., 102*, 201-212, 1997.

Ricard, Y., M. A. Richards, C. Lithgow-Bertelloni, and Y. L. Stunff, A geodynamic model of mantle density heterogeneity, *J. Geophys. Res., 98*, 21,895-21,909, 1993.

Richards, M. A., B. H. Hager, and N. H. Sleep, Dynamically supported geoid highs over hotspots: Observation and theory, *J. Geophys. Res., 93*, 7690-7708, 1988.

Shen, Y., S. C. Solomon, I. T. Bjarnason, and C. J. Wolfe, Seismic evidence for a lower-mantle origin of the Iceland plume, *Nature, 395*, 62-65, 1998.

Solomatov, V. S., Scaling of temperature- and stress-dependent viscosity convection, *Phys. Fluids, 7*, 266-274, 1995.

Steinberger, B. and R. J. O'Connell, Advection of plumes in mantle flow: Implications for hotspot motion, mantle viscosity and plume distribution, *Geophys. J. Int., 132*, 412-434, 1998.

Su, W. J. and A. M. Dziewonski, On the scale of mantle heterogeneity, *Phys. Earth Planet. Int.er., 74*, 29-54, 1992.

Tackley, P. J., Self-consistent generation of tectonic plates in 3-dimensional mantle convection, *Earth Planet. Sci. Lett., 157*, 9-22, 1998.

Tackley, P. J., Effects Of strongly variable viscosity on 3-dimensional compressible convection in planetary mantles, *J. Geophys. Res., 101*, 3311-3332, 1996.

Tackley, P. J., Effects of Strongly Temperature-Dependent Viscosity on Time-Dependent, 3-Dimensional Models of Mantle Convection, *Geophys. Res. Lett., 20*, 2187-2190, 1993.

Tackley, P. J., D. J. Stevenson, G. A. Glatzmaier, and G. Schubert, Effects of an endothermic phase-transition at 670 km depth in a

spherical model of convection in the Earth's mantle, *Nature, 361*, 699-704, 1993.

Turcotte, D. L. and G. Schubert, *Geodynamics*, 450 pp., John Wiley, New York, 1982.

VanDecar, J. C., D. E. James, M. Assumpcao, Seismic evidence for a fossil mantle plume beneath south-America and implications for plate driving forces, *Nature, 378*, 25-30, 1995.

van der Hilst, R. D., and H. Karason, Compositional heterogeneities in the bottom 1000 kilometers of Earth's mantle: Toward a hybrid convection model, *Science, 283*, 1885-1888, 1999.

van der Hilst, R. D., S. Widiyantoro, and E. R. Engdahl, Evidence for deep mantle circulation from global tomography, *Nature, 386*, 578-584, 1997.

Van der Voo, R., W. Spakman, and H. Bijwaard, Mesozoic subducted slabs under Siberia, *Nature, 397*, 246-249, 1999.

Wolfe, C. J., I. T. Bjarnason, J. C. Vandecar, and S. C. Solomon, Seismic structure of the Iceland mantle plume, *Nature, 385*, 245-247, 1997.

Zhang, S., and D. A. Yuen, The influences of lower mantle viscosity stratification on 3-D spherical-shell mantle convection, *Earth Planet. Sci. Lett., 132*, 157-166, 1995.

Zhang, Y. S., and T. Tanimoto, Ridges, hotspots and their interaction as observed in seismic velocity maps, *Nature, 355*, 45-49, 1992.

Zhong, S., and G. F. Davies, Effects of plate and slab viscosities on the geoid, *Earth Planet. Sci. Lett., 170*, 487-496, 1999.

Zhong, S., and M. Gurnis, Interaction of weak faults and non-Newtonian rheology produces plate tectonics in a 3D model of mantle flow, *Nature, 383*, 245-247. 1996.

Zhong, S., and M. Gurnis, Dynamic feedback between an non-subducting raft and thermal convection, *J. Geophys. Res., 98*, 12219-12232, 1993.

Zhong, S., and M. Gurnis, The role of plates and temperature-dependent viscosity in phase change dynamics, *J. Geophys. Res., 99*, 15,903-15,917, 1994.

Zhong, S., and M. Gurnis, Mantle convection with plates and mobile, faulted plate margins, *Science, 267*, 838-843, 1995.

Zhong, S., M. Gurnis, and L. Moresi, The role of faults, nonlinear rheology, and viscosity structure in generating plates from instantaneous mantle flow models, *J. Geophys. Res., 103*, 15255-15268, 1998.

M. Gurnis, Seismological Laboratory, California Institute of Technology, Pasadena, CA 91125.

L. Moresi, Australian Geodynamics Cooperative Research Centre, CSIRO, Exploration and Mining, 39, Fairway, Nedlands 6009, Western Australia, Australia.

S. Zhong and M. T. Zuber, Department of Earth, Atmospheric, and Planetary Sciences, Massachusetts Institute of Technology, Cambridge, MA 02139. (szhong@rayleigh.mit.edu)

(Received July 16, 1999; revised January 1, 2000;
accepted January 6, 2000.)